Q. J. R. Meteorol. Soc. (2000), **126**, pp. 3343–3369

Atmosphere–ocean thermal coupling in the North Atlantic: A positive feedback

By M. WATANABE* and M. KIMOTO
University of Tokyo, Japan

(Received 4 January 2000; revised 12 June 2000)

SUMMARY

In this article, it is examined whether a positive atmosphere–ocean feedback is found over the North Atlantic through a series of general circulation model (GCM) experiments.

A 60-year integration of an atmospheric GCM (AGCM) coupled with a 50 m deep motionless ocean was conducted. The coupled run was compared with two uncoupled runs, one with prescribed mid-latitude climatological sea surface temperatures (SSTs) and the other with daily SSTs derived from the coupled experiment. The uncoupled atmosphere forces the slab ocean, to obtain SST responses in these runs. Consistent with previous studies, the coupled atmosphere–ocean fields show interannual variances larger than those in the uncoupled runs, due to reduction in the local thermal damping.

Patterns of maximum atmosphere–ocean covariability show the North Atlantic Oscillation (NAO) and tripole SST anomalies both in the coupled and uncoupled fields, indicating a dominant role of the atmosphere in generating the SST anomalies. On the other hand, analyses of the temporal variability in the three runs suggest an active role of SST anomalies in determining the polarity of the air–sea coupled variability longer than the interannual time-scale. A combined analysis of forcing SST, upper-air height, and the response SST anomalies in the uncoupled run identified that a patch of positive SST anomalies in the mid-latitude band around 40°N effectively excite the positive phase of the NAO, which in turn reinforces the tripole SST anomalies. This relationship was further confirmed by a nine-member ensemble AGCM experiment forced by the relevant SST anomalies. Since the forcing and response SST anomaly patterns bear some resemblance, these results manifest positive feedback at work in the coupled atmosphere–ocean patterns. The processes responsible for this positive feedback were elaborated by a series of linear model experiments. The local thermal adjustment of the atmosphere to the SST anomalies results in increased precipitation over the Gulf Stream region. Associated diabatic heating applied to a linear baroclinic model yields a positive height response to the east, which highly influences the southern part of the NAO. This stationary response in turn induces a northward deflection in the storm track activity, leading to an eddy vorticity feedback that tends to force the positive phase of the NAO.

KEYWORDS: Mid-latitude air–sea interaction North Atlantic Oscillation Tripole sea surface temperature anomaly

1. INTRODUCTION

Several decades ago, Bjerknes (1964) first found a coupled atmosphere–ocean variability over the North Atlantic using mean-sea-level pressure (m.s.l.p.) and sea surface temperature (SST) datasets. The coupled pattern identified consists of a dipole of m.s.l.p., often referred to as the North Atlantic Oscillation (NAO), and SST anomalies having opposite polarity in the Gulf Stream region and to the south of Greenland. After Bjerknes, observational studies so far conducted suggest that SST anomalies in middle latitudes are mainly driven by the atmosphere through surface heat flux anomalies (Wallace *et al.* 1990; Cayan 1992). The basic concept of this atmospheric driving of the ocean in middle latitudes has been verified by a stochastic theory (Frankignoul 1985). In the North Atlantic, it is now well known that the NAO and a tripole SST anomaly pattern are identified as a statistically derived coupled variability (e.g. Wallace *et al.* 1992). Observational analyses, such as the lag correlations, suggest that the latter is the response to the former.

On the other hand, a number of studies using atmospheric general circulation models (AGCMs) have addressed the question whether North Atlantic SST anomalies have an impact on the atmospheric circulation (Palmer and Sun 1985; Ferranti *et al.* 1994; Peng *et al.* 1995; Kushnir and Held 1996; Rodwell *et al.* 1999). Most of the atmospheric responses to mid-latitude positive SST anomalies found in their experiments show

* Corresponding author: Center for Climate System Research, University of Tokyo, 4-6-1 Komaba, Meguro, Tokyo 153-8904, Japan. e-mail: hiro@ccsr.u-tokyo.ac.jp

shallow baroclinicity near the SST anomaly and a downstream ridge with an equivalent barotropic structure. However, these responses are weak and not robust because of the sensitivity to the model resolution and its climatology (Peng *et al.* 1997), and also to the transient eddy feedback (Peng and Whitaker 1999).

Since SSTs are prescribed in the above experiments, their results may not be directly applicable to the role of active SSTs in the real coupled system. In this regard, the role of atmosphere–ocean coupling, or the effect of interactive SSTs, has recently been explored using coupled atmosphere–ocean models (Manabe and Stouffer 1996; Bladé 1997; Barsugli and Battisti 1998; Saravanan 1998; Bhatt *et al.* 1998). Because the thermal, rather than momentum, exchange at the atmosphere–ocean interface is a dominant source for the coupled variability in middle latitudes, some of the models employ a simple motionless ocean. The experiments commonly show a quite significant result: atmosphere–ocean coupling increases thermal variances, in both the atmosphere and oceans, at interannual or longer time-scales. The coupling results in an adjustment between the atmosphere and oceans, leading to a reduction in the net surface heat flux that works as a damping for both media. This effect, called the *reduced thermal damping* by Barsugli and Battisti (1998), extends the persistence of the atmospheric anomalies (Bladé 1997), and sometimes 'reorders' the dominant modes in the free atmosphere (Saravanan 1998). However, the concept of the reduced thermal damping alone is not sufficient to tell us about the processes controlling temporal characteristics and the polarity of the coupled variability.

An ensemble simulation of The UK Met. Office's AGCM by Rodwell *et al.* (1999) gives a useful insight into this question. They succeeded in reproducing the interannual to decadal fluctuation of the NAO by prescribing observed SSTs in the model. They found that the positive (negative) evaporation anomalies over the positive (negative) SST anomalies induce precipitation anomalies *in situ*, and the associated diabatic heating forces the NAO-like geopotential height anomalies. The evaporation anomalies in turn act to damp the SST anomalies, i.e. the negative feedback. If we consider a coupled system, however, the NAO-like response may further increase the SST anomalies that form a positive atmosphere–ocean feedback loop. To make clear the possibility of this positive feedback is particularly important in theoretical considerations regarding the mid-latitude decadal-scale climate variability, in which a crucial role of the feedback in generating decadal periodicity is expected (e.g. Münnich *et al.* 1998; Weng and Neelin 1998; Neelin and Weng 1999; Watanabe and Kimoto 2000). Thus the purpose of this article is to investigate if the positive feedback is found in a coupled system and, furthermore, if it significantly contributes to determine the polarity of atmosphere–ocean coupled fluctuations over the North Atlantic. Recently, Venzke *et al.* (1999) performed an ensemble AGCM simulation for similar reasons. They detected an NAO-like m.s.l.p. response to a tripole SST anomaly pattern, both of which are known as a statistically derived coupled pattern in the North Atlantic, but a positive feedback between them only occurs to the south of Greenland.

As emphasized by Saravanan (1998), the atmosphere–ocean feedback process in middle latitudes is hardly detected in analyses of observational data alone, because of the dominant atmospheric forcing of the ocean. Therefore, here we conduct several numerical experiments using an AGCM coupled with a motionless 'slab' ocean. Through a comparison of the coupled run with two uncoupled runs, possibility of the positive feedback is examined. In section 2, the model and the experimental design are described. Preliminary analyses of variance in the coupled and uncoupled fields, which confirm findings in previous studies, are presented in section 3. In section 4, analysis is extended toward a detection of a positive atmosphere–ocean feedback. A combined

analysis of the coupled and uncoupled fields made it possible to identify an effective SST anomaly pattern which influences the polarity of the NAO and associated tripole SST anomalies. Because the former SST anomaly pattern has a large projection onto the tripole SST anomalies, this suggests the presence of positive feedback. In section 5, the positive feedback is further verified with an ensemble AGCM simulation which gives an estimate of the magnitude of the feedback, and atmospheric processes responsible for the feedback loop are then elaborated using linear dynamical models. A summary and discussion are given in section 6.

2. Model and experimental design

The atmospheric model used in this study is a global spectral GCM co-operatively developed at the Center for Climate System Research (CCSR), University of Tokyo, and the National Institute for Environmental Studies (NIES); this is referred to as the CCSR/NIES AGCM. The CCSR/NIES AGCM has standard physics such as: the Arakawa–Schubert cumulus parametrization, radiative transfer scheme, a bucket model for land surface processes, and the level 2.0 turbulence closure scheme by Mellor and Yamada (1974, 1982). One can find more details of the model in Numaguti *et al.* (1995), Shen *et al.* (1998), and Watanabe and Nitta (1998). Here a low-resolution version of this AGCM is used, namely, with horizontal resolution of T21 and 11 sigma levels in the vertical. As mentioned in the introduction, this model is coupled to a 50 m deep, motionless ocean in order to investigate the effect of atmosphere–ocean thermal coupling. The simple ocean does not include the ocean dynamics to generate El Niño in the equatorial Pacific, which may be necessary to simulate realistic variances not only in the tropical but also in the extratropical atmosphere. To avoid this problem, SSTs in the tropical band from 20°S to 20°N are prescribed as monthly SST observations. A flux correction is also applied outside the tropics in order to compensate for the ocean heat transport. The climatological flux is calculated using a 20-year integration of the coupled model in advance, by restoring the extratropical SSTs to observed values with a time constant of three days.

The coupled model was integrated for 60 years with observed tropical SSTs from January 1938 to December 1997 in the tropics. The design of this experiment follows the Tropical Ocean/Global Atmosphere mixed-layer (TOGA-ML) experiment by Lau and Nath (1996) who examined teleconnection processes in the Pacific. It is emphasized, however, that an historical simulation is not the aim of this study. In addition to this coupled run (hereafter referred to as CTL), two uncoupled experiments were conducted with tropical conditions identical to CTL. Atmospheric fields in both experiments are driven by prescribed SSTs (often referred to as the *forcing* SSTs, hereafter) even in middle latitudes, as schematically illustrated in Fig. 1. Given archived extratropical SSTs in CTL, one uncoupled run employs the same climatology, while daily values are provided to the other (cf. Fig. 1). These uncoupled experiments are called PS1 and PS2 runs, respectively. The atmosphere in these runs forces the passive slab ocean to compute *response* SSTs. It should be noted that the net surface heat fluxes from the ocean (O) to the atmosphere (A; denoted as $Q^{\mathrm{U}}_{\mathrm{OA}}$; the superscript 'U' stands for 'uncoupled') and vice versa ($Q^{\mathrm{U}}_{\mathrm{AO}}$) are not the same as each other in the uncoupled runs.

Barsugli and Battisti (1998) have discussed differences in temperature variances in the above three systems but with a much simplified energy-balance model. Their results have been verified further by other studies which used GCMs (Bladé 1997; Saravanan 1998; Bhatt *et al.* 1998). While the focus of this study is to investigate if a positive atmosphere–ocean feedback plays a role in the coupled variability, we first present the

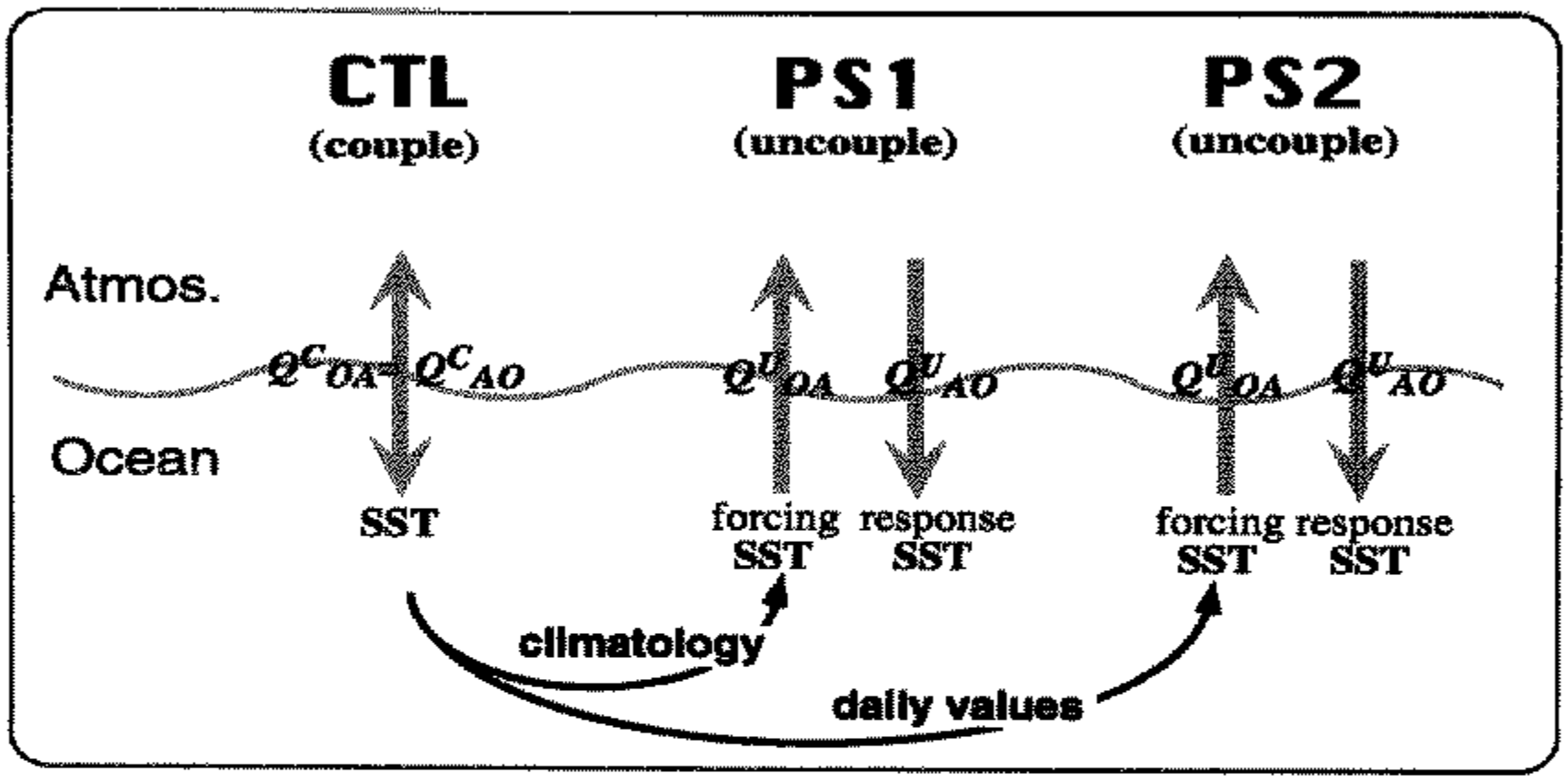

Figure 1. Schematic diagram showing designs for three GCM experiments (see text for description).

analysis of variance in the next section in order to confirm findings in the previous studies. Since we mainly concentrate on the wintertime (December–February) fields, when the atmosphere shows the largest anomalies, seasonality of the coupled variability is not discussed. While observed fields are not thoroughly analysed in this study, the extent to which the analysis of simulated fields are applicable to the real climate will be remarked (cf. sections 4(a), 5(b), and 6).

3. Change in low-frequency variances

Changes in the atmosphere–ocean variance with and without thermal coupling are first evaluated in terms of standard deviations (SDs) of the winter 500 hPa height (hereafter referred to as Z500) and SST anomalies (response SSTs in the uncoupled runs). Figure 2(a) and (d) show SDs of these quantities over the North Atlantic in CTL. The pattern of Z500 (Fig. 2(a)) shows a meridional dipole having maxima of about 65 m, which reflects a dominant mode of variability over the domain, i.e. the NAO. This pattern is realistic compared to observations such as the NCEP/NCAR* re-analysis (not shown), but the variability north (south) of 50°N is somewhat underestimated (overestimated) in the model. The SD in winter SST fields (Fig. 2(d)) represents large variances in the north-western part of the North Atlantic, including the vicinity of the Gulf Stream. While this is consistent with the observational counterpart (e.g. winter Global Ice and SST (GISST) fields, not shown), the simulation shows the maximum to the south of Greenland while the observations show much variability along the Gulf Stream. The difference in the location of the maximum variance is attributed to the lack of ocean dynamics in CTL.

When SDs of Z500 fields from the uncoupled runs are compared with those of CTL (Fig. 2(b) and (c)), a decrease in the SD of about 10 m is found over a large part of the North Atlantic. While the height variances increase over eastern Canada and northern Europe, the SDs in these areas are minimal in the model. A similar comparison made for SST fields (Fig. 2(e) and (f)) shows that the SST variances in PS1 and PS2 are lower than those in CTL over the entire North Atlantic. These figures indicate that the thermal coupling in middle latitudes enhances the variance both in the atmosphere and in the ocean. However, the decrease in SDs of Z500 and SST is more conspicuous in PS1 than

* National Centers for Environmental Prediction/National Center for Atmospheric Research.

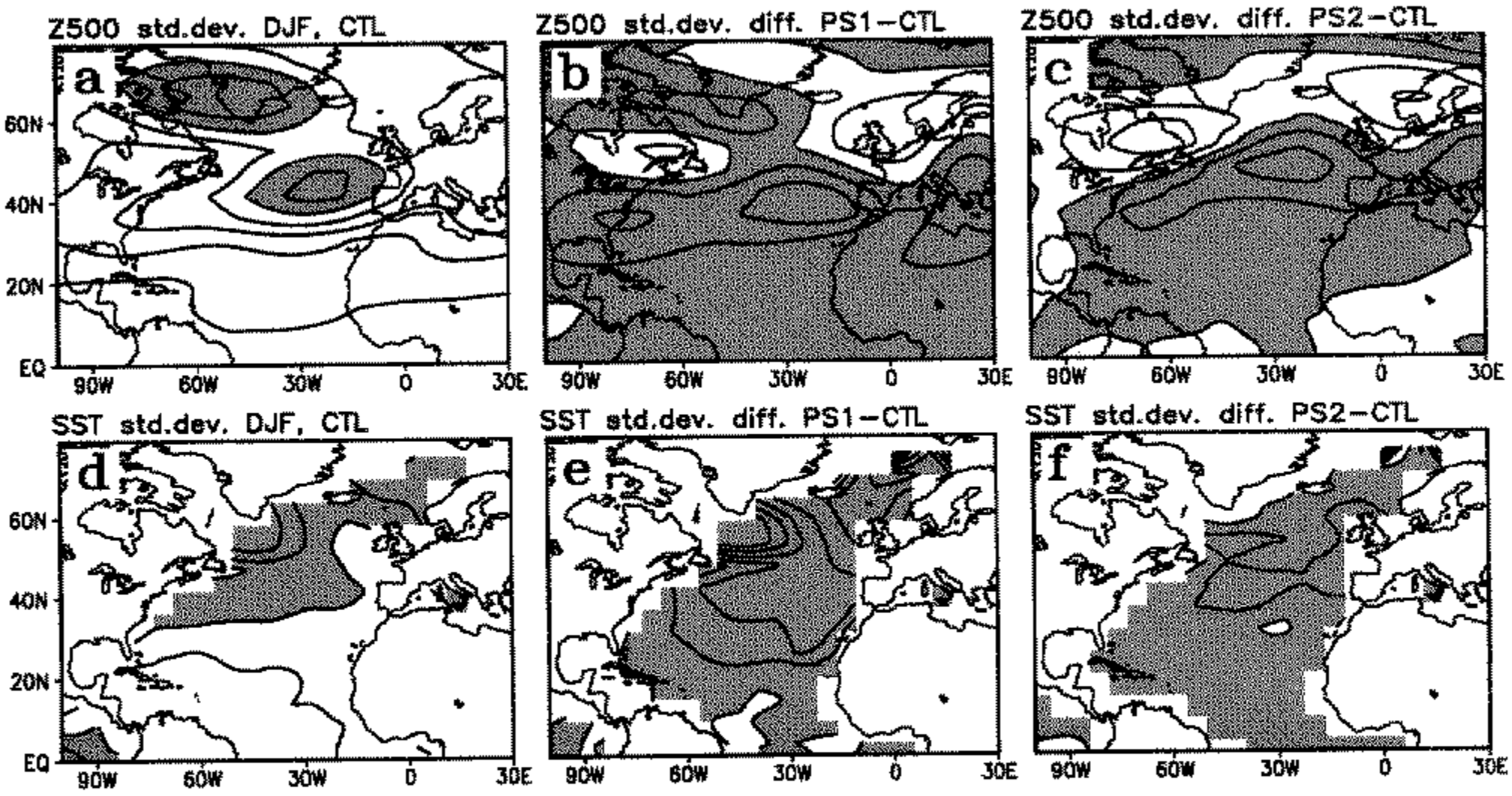

Figure 2. (a) Standard deviations (SDs) for winter 500 hPa height anomalies over the North Atlantic in the coupled general circulation model experiment, CTL. Contour interval is 10 m while values greater than 50 m are shaded. (b) Differences in the height SDs between CTL and uncoupled experiment PS1. Contour interval is 5 m with negative values shaded. (c) As (b) but for differences between CTL and uncoupled experiment PS2. (d)–(f) As (a)–(c) but for winter sea surface temperature anomalies. Contour intervals are 0.2 K in (d) and 0.1 K in (e) and (f). The shading in (d) denotes values greater than 0.6 K. See text for details of models.

in PS2. Similar results have been reported in previous studies (Manabe and Stouffer 1996; Bladé 1997; Barsugli and Battisti 1998; Bhatt *et al.* 1998).

As mentioned in the introduction, Barsugli and Battisti (1998) have explained the essential physics responsible for the enhanced variance in the coupled system in terms of the reduction of the heat flux variance due to atmosphere–ocean adjustment. Their theory shows that this adjustment is more effective on time-scales longer than several months which is the e-folding time for mixed-layer temperature anomalies in the mid-latitude ocean. In order to verify their results in our experiments, we present power spectra for the net surface heat flux averaged over the North Atlantic in Fig. 3(a) and (b). The spectra for CTL ($Q^{\mathrm{C}}_{\mathrm{AO}} = Q^{\mathrm{C}}_{\mathrm{OA}}$, thick solid lines; the superscript 'C' stands for 'coupled') are roughly flat in the frequencies higher than 1 cpy while they drop off in the lower frequencies toward zero due to adjustment of SSTs to the atmospheric conditions. The slope in lower-frequency bands is similarly found in the spectra for $Q^{\mathrm{U}}_{\mathrm{AO}}$ in PS1 and PS2 (Fig. 3(a)) because it is calculated using atmospheric quantities and adjusted SSTs. On the other hand, spectra for $Q^{\mathrm{U}}_{\mathrm{OA}}$ (Fig. 3(b)) show different shapes from those for $Q^{\mathrm{C}}_{\mathrm{OA}}$ in CTL and $Q^{\mathrm{U}}_{\mathrm{AO}}$ in the uncoupled runs; they are flat in all frequencies in PS1, but increase in low frequencies in PS2.

The spectra shown in Fig. 3(a) and (b) are quite similar to Figs. 7 and 10(b) of Barsugli and Battisti (1998), therefore the above results support their interpretation. However, one controversy is found in Fig. 3(b). The power spectrum for $Q^{\mathrm{U}}_{\mathrm{OA}}$ in PS2 clearly shows larger variance than that in PS1 on interannual time-scales, which should imply larger damping for the PS2 atmosphere. Nevertheless, the spectrum for $Q^{\mathrm{U}}_{\mathrm{AO}}$ in PS2 reveals low-frequency variance nearly identical to that for the net flux spectrum in CTL, and larger than that in PS1. In our simple ocean, this difference is directly reflected in the variability in SST, so that the spectra show a similar difference, i.e. CTL > PS2 $\gg$ PS1 (Fig. 3(c)). Recall that PS2 employs time-dependent prescribed SSTs in the

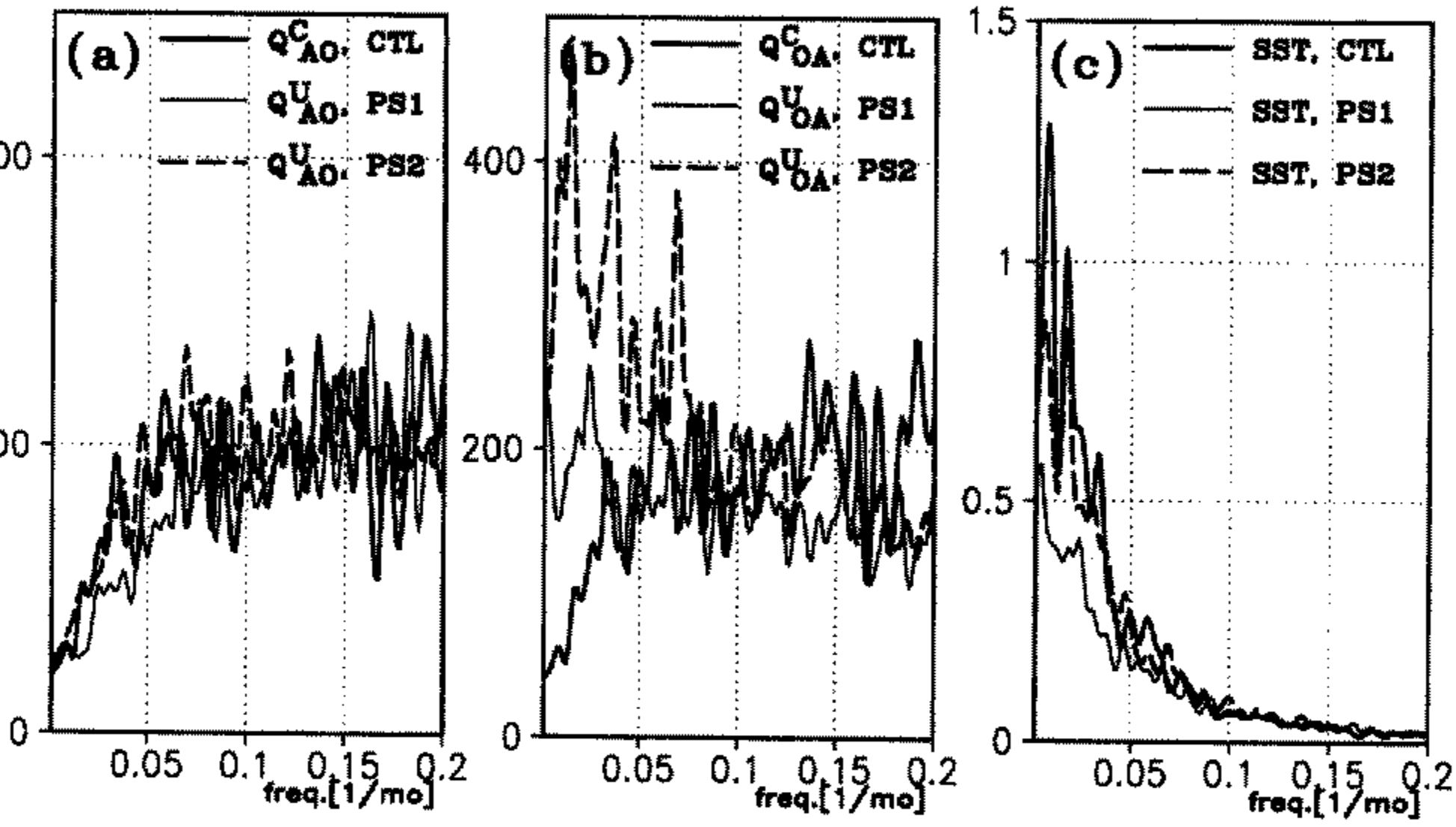

Figure 3. (a) Power spectra of monthly net surface fluxes from the atmosphere to the ocean (Q^C_{AO} and Q^U_{AO}) averaged over 0°–100°W and 20°–70°N in the coupled (superscript C; CTL) general circulation model experiment, and uncoupled (superscript U; PS1 and PS2) runs. (b) As (a), but for heat fluxes from the ocean to the atmosphere (Q^C_{OA} and Q^U_{OA}). Note that Q^C_{OA} is equal to Q^C_{AO} in CTL. (c) As (a), but for monthly sea surface temperature anomalies. See text for details of models.

extratropics, differences in the spectra for Q^U_{OA} and SST between PS1 and PS2 suggest that the effect of SST anomalies on the atmosphere–ocean system should induce aspects other than the reduced thermal damping. In the next section the difference between PS1 and PS2 is examined in terms of the temporal fluctuations in Z500 and SST, together with their coherence with CTL.

4. Simulated coupled variability

(a) *Atmosphere–ocean coupled patterns*

The reduced thermal damping effect shown in the previous section is essentially a local process. On the other hand, a positive feedback between the atmosphere and the ocean, if any, possibly involves non-local processes. In order to discuss such processes, a coupled pattern of variability should first be identified. Here we employ the singular value decomposition (SVD) analysis to detect an atmosphere–ocean coupled variability (Bretherton *et al.* 1992). The SVD analyses are applied to winter Z500 and SST anomalies in the three GCM experiments, and additionally to the NCEP/NCAR re-analysis and GISST during 1958–97. It is noted that the leading modes in the four pairs of fields, which are described below, are all statistically significant at the 95% level based on a Monte Carlo test (Iwasaka and Wallace 1995).

Shown in Fig. 4(a) are the leading SVDs in the GISST/NCEP fields represented by the heterogeneous regression maps, which account for 41% of the total covariance. The coupled pattern in observations is already familiar (cf. Wallace *et al.* 1992) having a Z500 dipole and a tripole SST pattern. It should be noted that the Z500 dipole shown in Fig. 4(a) somewhat resembles the NAO, but the relative magnitudes of the northern and southern centres are uneven, and the node is shifted to the south by 10 degrees compared to the canonical NAO (e.g. Barnston and Livezey 1987). While the leading SVD in CTL also shows a Z500 dipole and a SST tripole (Fig. 4(b)), there are several

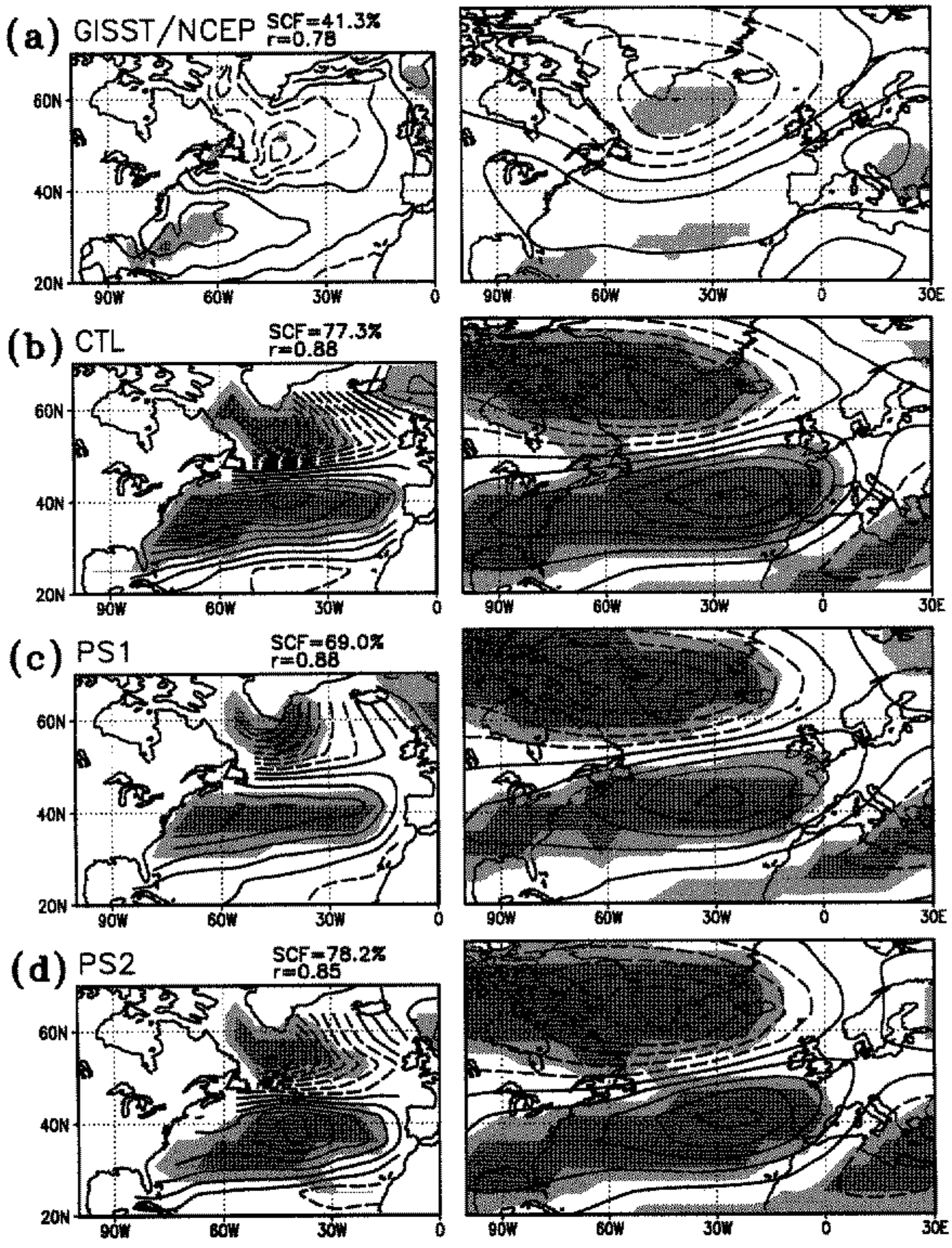

Figure 4. Heterogeneous regression maps for the leading singular value decomposition mode between winter sea surface temperature (SST; left panels) and 500 hPa height (right panels) anomalies over the North Atlantic in: (a) observations (GISST and NCEP/NCAR re-analysis for 1958–97), (b) coupled experiment CTL, and uncoupled experiments (c) PS1, and (d) PS2. Note that response SST is used in PS1 and PS2. Squared covariance fraction (SCF) and the correlation coefficient between expansion coefficients (r) are shown at the top of left panels. Contour intervals for SST and height regressions are 0.1 K and 10 m, respectively, while the negative contours are dashed. Statistically significant areas at the 95 (99)% level are indicated by the light (dark) shading. See text for further details.

discrepancies with the observed mode. The most apparent difference is that the dipole in the height anomalies is more projected on to the model's NAO as defined by the leading empirical orthogonal function (EOF) of monthly Z500 anomalies (not shown, see also appendix A), leading to higher significance of the mode in CTL than in observations. The SST regressions also reveal positive anomalies in the 30°–45°N latitude band, more zonally elongated in the model, observations being confined to the US east coast.

The leading SVDs in the two uncoupled runs, between the Z500 and the response SSTs, are shown in Fig. 4(c) and (d). They account for 69 and 78% of the total covariance in the respective fields. It should be noted that the patterns show little difference from the leading SVD in CTL, indicating that these coupled patterns are primarily driven by the atmosphere because response SSTs in PS1 and PS2 are passive. The similarity between the leading SVDs in three experiments also indicates that neither the coupling nor the presence of anomalies in forcing SSTs modify the spatial structure of the dominant atmosphere–ocean coupled fluctuation. This result is again consistent with previous reports (Bladé 1997; Saravanan 1998). However, the squared-covariance fraction (SCF) in PS1 is the lowest among the three experiments, while SCFs in the other two are comparable. This may imply that the SST anomalies in the North Atlantic preferentially enhance the NAO-like atmospheric anomalies.

(*b*) *Temporal coherence*

Observational studies (Frankignoul 1985; Cayan 1992) and the SVD analysis shown in section 4(a) suggest that the substantial part of the coupled atmosphere–ocean variability is due to the variability in the free atmosphere independent of SST anomalies. If, however, even a part of such forced SST anomalies reinforces the atmospheric variability, such a feedback may affect the temporal variability of the large-scale patterns. As referred to in the introduction, an AGCM study by Rodwell *et al.* (1999) does show the active role of mid-latitude SST anomalies in simulating the temporal variability of the NAO. In our experiments, the active role of SST anomalies is first examined by cross-spectrum and correlation analyses between Z500 and SST in the coupled and uncoupled runs.

Coherence spectra between monthly anomalies of SST in CTL and response SSTs in PS1 at individual grid points are averaged over the North Atlantic (Fig. 5(a)). Due to the identical prescribed SSTs in the tropics, SST anomalies in the two runs have coherence of about 0.2 with the SD about 0.1 (shading) at all the frequencies. Strong coherence in a specific frequency band is not found in Fig. 5(a). On the other hand, the coherence spectrum between SST anomalies in CTL and PS2 clearly shows an increase of coherence at frequencies lower than 1 cpy (Fig. 5(b)). Since the SSTs in CTL force the PS2 atmosphere, enhanced low-frequency coherence shown in Fig. 5(b) strongly suggests that the atmosphere affected by an SST anomaly tends to reinforce it, namely, it produces positive feedback. The phase spectrum corresponding to Fig. 5(b), indicating the lead of SST anomalies in CTL for several months, reinforces the feedback (not shown). Although the change in the shape of coherence spectra in PS1 and PS2 is less dominant for Z500 anomalies (Fig. 5(c) and (d)), an enhancement of coherence at interannual to decadal time-scales is also visible.

Spatial locations responsible for the enhanced low-frequency coherence (Fig. 5) are identified by calculating local correlation coefficients between CTL and two uncoupled (i.e. PS1 and PS2) fields (not shown). The correlation map between monthly SST anomalies in CTL and PS1 is again different from that between CTL and PS2, such that the latter shows highly significant positive correlations in most part of the North Atlantic except for the coastal regions. Unlike SST anomalies, correlations of Z500 anomalies between CTL and the two uncoupled fields are similarly insignificant in the extratropics. However, when a 24-month low-pass filter is applied to Z500 anomalies, significant correlations are found over the ocean, except for the region off Newfoundland with the node of the NAO, suggesting the increased coherence in Fig. 5(d) compared to Fig. 5(c) is due to coherence of the NAO. In fact, time coefficients of the leading EOF for monthly Z500 anomalies in CTL and PS2, both of which well represent the NAO

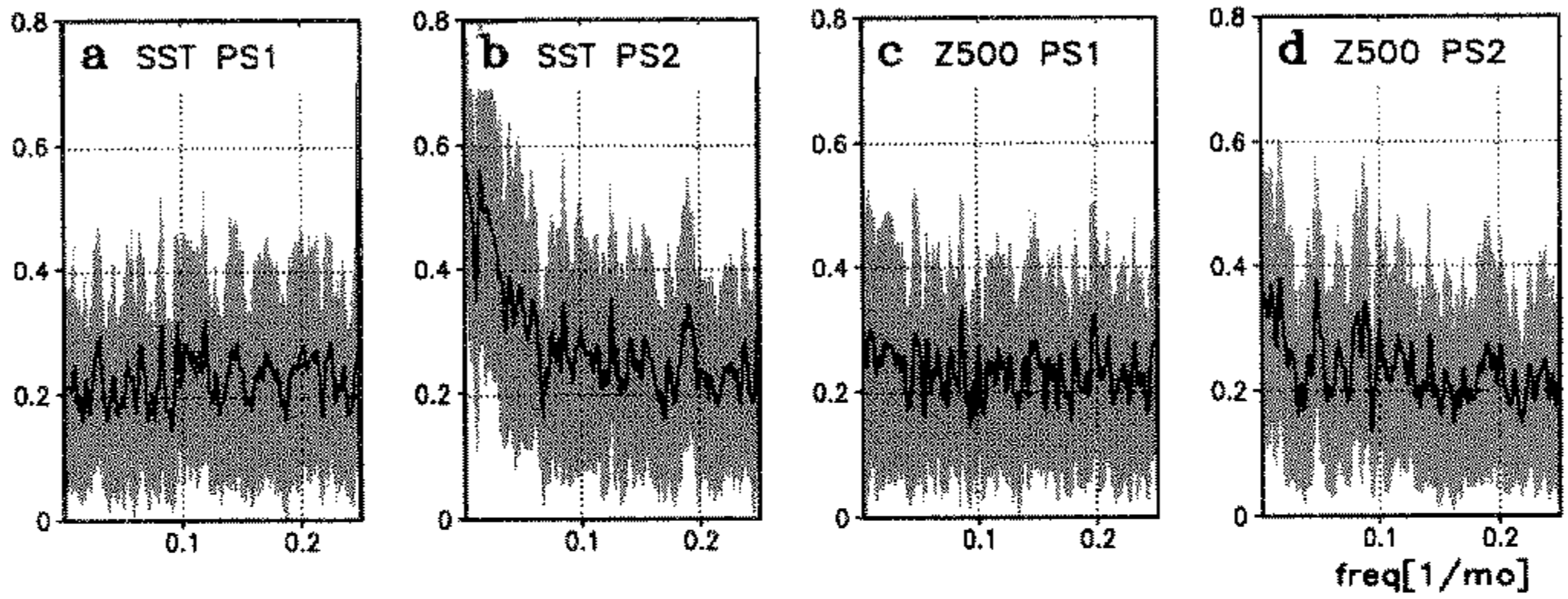

Figure 5. (a) Coherence between monthly sea surface temperature (SST) anomalies in coupled experiment CTL and uncoupled experiment PS1 averaged over 0°–100°W and 20°–70°N (thick line) with one standard deviation over the domain shown by the shading. (b) As (a), but for monthly SST anomalies in CTL and uncoupled experiment PS2. (c) And (d) as (a) and (b), but for the coherences between 500 hPa height anomalies. See text for details of models.

(see appendix A), are less correlated (0.11), while the correlation between the low-pass filtered time coefficients increases to 0.35 which is significant at the 95% level. In the next section, we attempt to identify the SST anomaly pattern which most effectively excites the dominant mode in the atmosphere, such as the NOA.

(c) *Detection of effective SST forcing*

In section 4(a), the SVD was used to identify the coupled pattern with the NAO-like Z500 anomalies and the tripole (response) SST anomaly pattern. Here the SVD analysis is extended to detect a SST forcing pattern which is the most effective in exciting this coupled pattern. For this purpose, a covariance matrix to be solved by the SVD, denoted as $\mathbf{C}_{SZ}$, is redefined using PS2 fields as

$$\mathbf{C}_{SZ} = (\mathbf{S}_{FRC}|\mathbf{S}_{RES})\mathbf{Z}^{T}, \tag{1}$$

where $\mathbf{S}_{FRC}$ and $\mathbf{S}_{RES}$ are winter forcing and response SST anomalies, respectively, in the North Atlantic, while $\mathbf{Z}$ denotes winter Z500 anomalies. This SVD, called combined SVD (CSVD) analysis for convenience, yields heterogeneous regression maps for $\mathbf{S}_{FRC}$, $\mathbf{S}_{RES}$, and $\mathbf{Z}$ with respect to each mode. The leading CSVD mode accounts for 72.4% of the total covariance with correlation between the expansion coefficients (r) of 0.54, and has a spatial structure as shown in Fig. 6.

The heterogeneous regressions for Z500 and response SST anomalies in PS2 (Fig. 6(a) and (c)), showing a pattern quite similar to the leading conventional SVD mode Fig. 4(d)), are highly significant. The regressions for forcing SST anomalies in PS2 (Fig. 6(b)) reveal a positive SST anomaly pattern along 40°N, although it is less significant than patterns on to the other two frames. These regression maps may be interpreted as follows: a forcing SST anomaly pattern shown in Fig. 6(b) excited the positive phase of the NAO (Fig. 6(a)), and that in turn fed back on the ocean to generate the tripole SST response (Fig. 6(c)). This view, however, may not seem very convincing because the spatial significance of the forcing SST anomalies is insufficient. To make clearer the statistical robustness of the forcing SST pattern (Fig. 6(b)) and the NAO–tripole SST relationship, a Monte Carlo test was performed for the singular value and r of the leading CSVD mode (Fig. 7). The test consists of computing singular modes for $\mathbf{S}_{FRC}$ randomly shuffled in time in Eq. (1). Figure 7 shows leading singular values

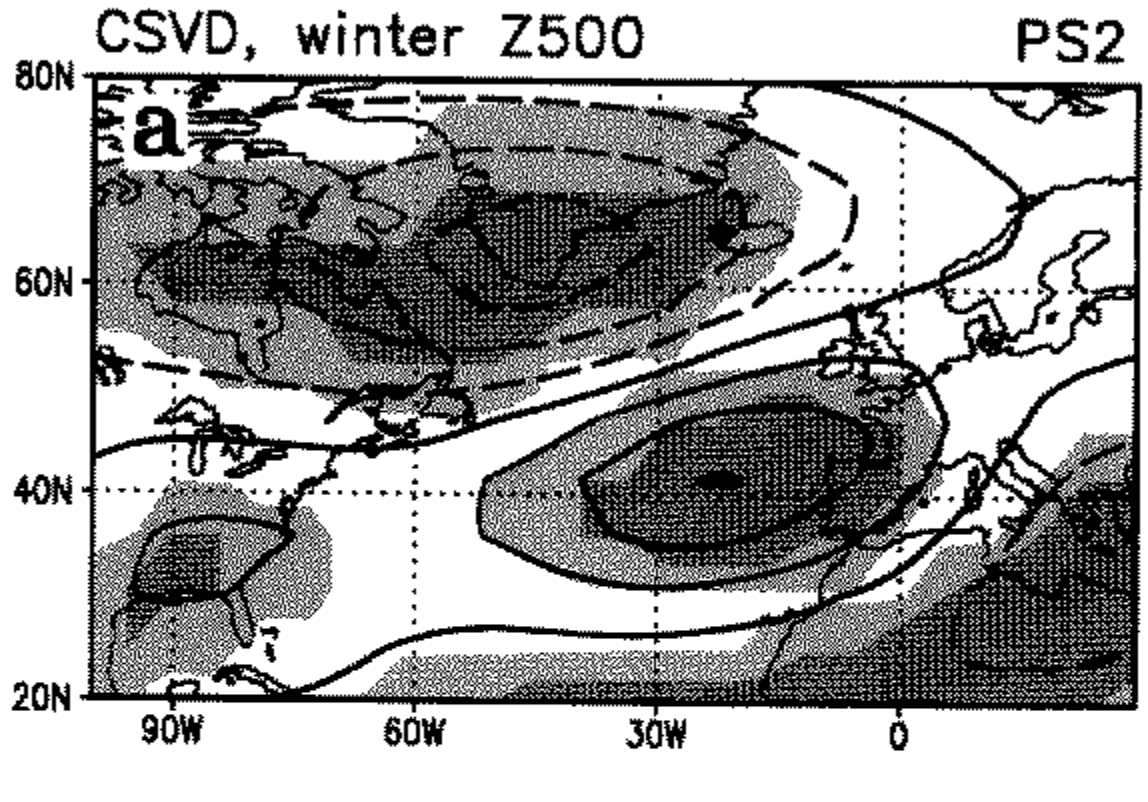

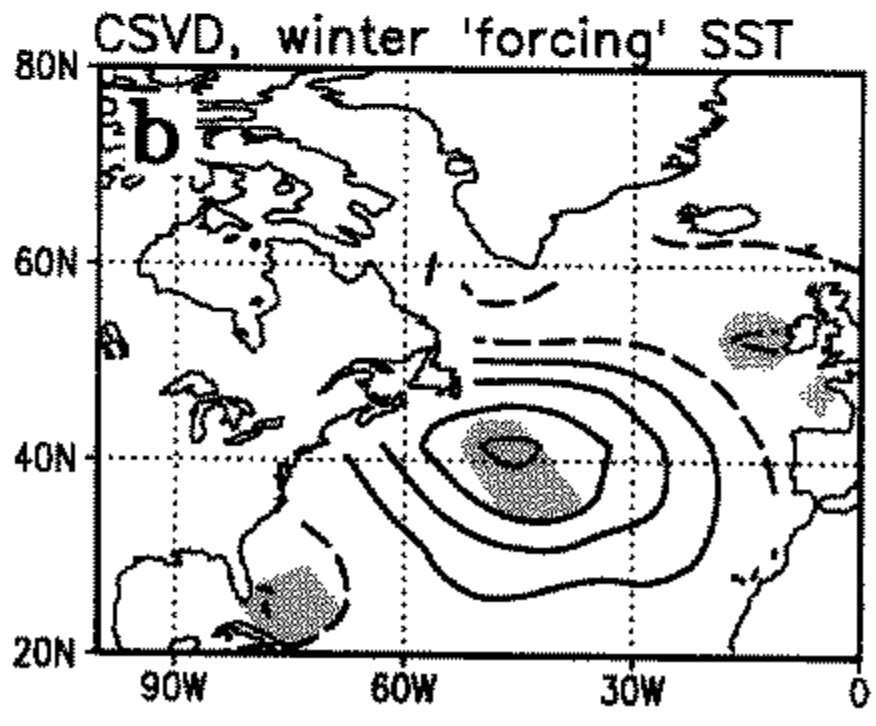

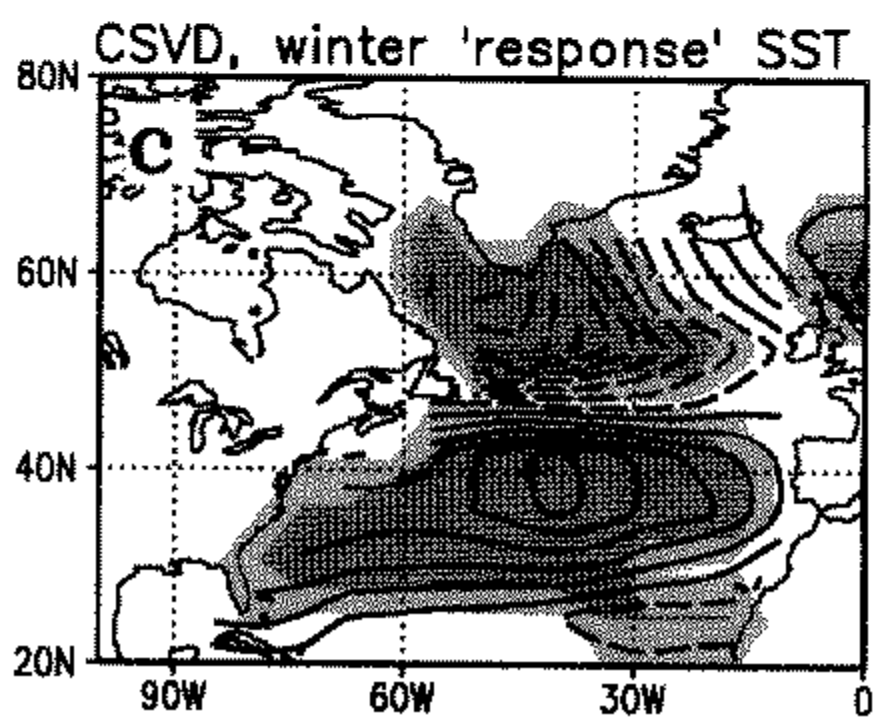

Figure 6. Heterogeneous regressions for the leading combined singular value decomposition (CSVD) mode in the winter uncoupled experiment PS2 fields. (a) 500 hPa height, (b) prescribed forcing sea surface temperature (SST) anomalies which are obtained from coupled experiment CTL (cf. Fig. 1), and (c) response SST anomalies calculated in PS2. Other details are as in Fig. 4. See text for descriptions of models.

and r obtained from the 200 random realizations, together with the respective quantity for the leading CSVD mode denoted by '×'. It is found that both the singular value (and r) are above 2 SD of the 200 realizations in which only two (four) are in excess of the singular value (r) for the leading CSVD mode, meaning it is significant at the 99% (98%) level. This result indicates that the relationship shown in Fig. 6 is, at least statistically, confidently established. The physical implication of the leading CSVD mode is investigated in sections 4(d) and 5. It is emphasized that the extent to which the forcing SST anomaly influences the NAO is much smaller than the atmospheric driving of the tripole SST anomalies, as represented by changes in probability densities of the patterns (see appendix A). It should be noted that the forcing SST pattern in Fig. 6(b) is quite similar to SST anomalies that Palmer and Sun (1985) dealt with in their pioneering work (see discussion in section 6).

(*d*) *Surface flux and precipitation anomalies*

To confirm further the presence of positive feedback in the mid-latitude SST anomalies as suggested so far, physical processes should be elaborated. In reality, the atmosphere will respond to the anomalous SST through surface flux and precipitation anomalies. Thus anomaly maps for the net heat flux and precipitation in PS2 were prepared based on a composite of winters when the SST expansion coefficients for the leading CSVD mode exceed ±1 SD. For comparison, similar composites are computed for the PS1 fields based on the SST expansion coefficients for the leading SVD mode in PS1 shown in Fig. 4(c). The composites for the two net fluxes, $Q^{\mathrm{U}}_{\mathrm{AO}}$ and $Q^{\mathrm{U}}_{\mathrm{OA}}$, are shown

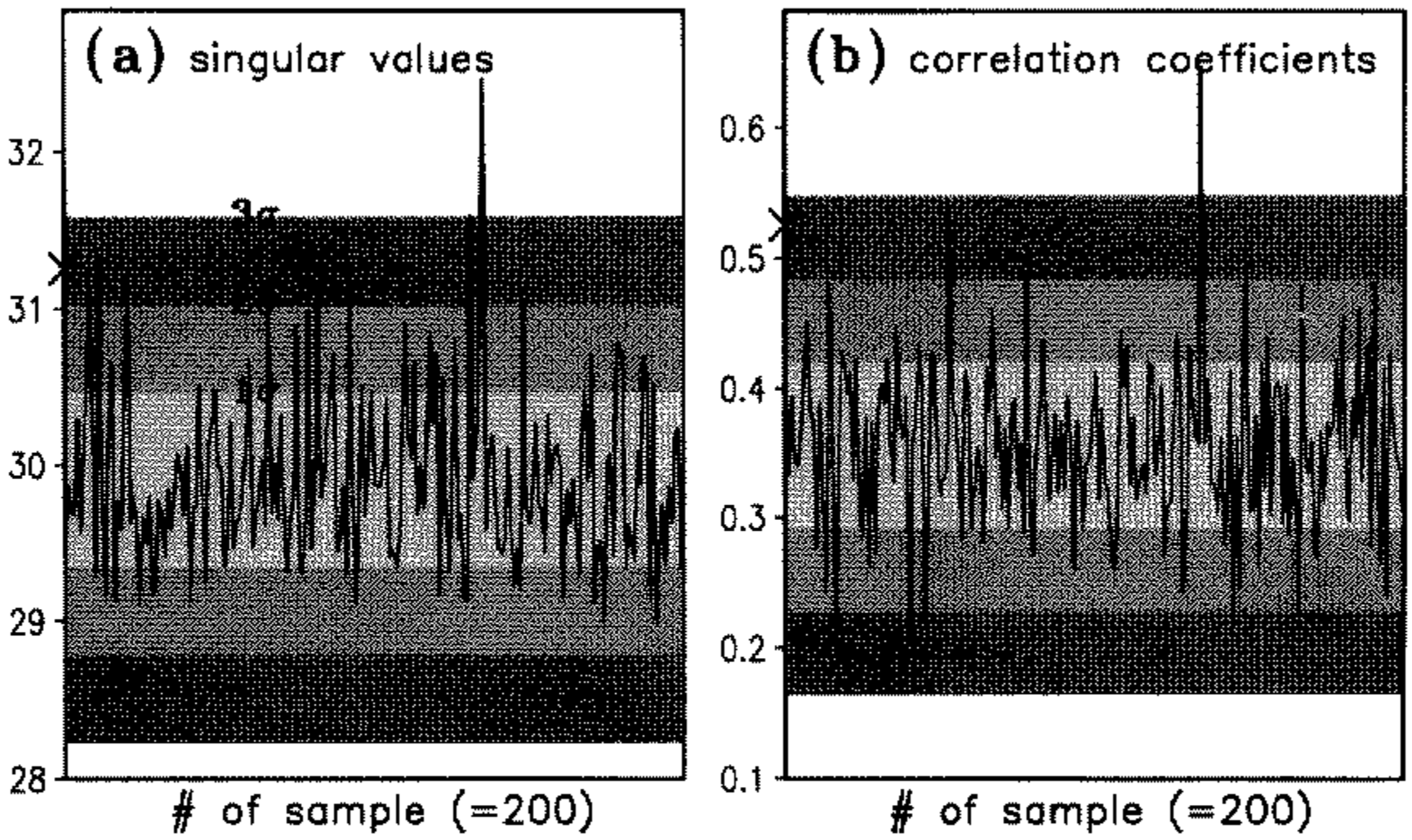

Figure 7. Results of the Monte Carlo test for the significance of the leading combined singular value decomposition (CSVD) mode shown in Fig. 6. Shown are (a) singular values and (b) correlation coefficients between expansion coefficients for the 200 random samples with their standard deviations. Values for the leading CSVD mode are indicated by '×' at the left of panels. See text for further details.

in Fig. 8, in which all the positive values denote a heat release from the ocean to the atmosphere. Keeping the experimental design in mind (cf. Fig. 1), it is expected that the composite anomalies for $Q_{\mathrm{AO}}^{\mathrm{U}}$ and $Q_{\mathrm{OA}}^{\mathrm{U}}$ in PS1 are similar to each other (Fig. 8(a) and (b)). They show a pattern which tends to generate the SST tripole, namely, warming of the ocean due to negative fluxes in middle latitudes with simultaneous cooling due to positive fluxes to the south of Greenland and in the subtropics. The fact that the composites for $Q_{\mathrm{OA}}^{\mathrm{U}}$ (Fig. 8(b)) have anomalies roughly three times as large as those for $Q_{\mathrm{AO}}^{\mathrm{U}}$ (Fig. 8(a)) is explained in terms of the lack of the thermal adjustment of SST in the former (cf. Fig. 3(b)), leading to larger air–sea temperature differences.

Composite anomalies for $Q_{\mathrm{AO}}^{\mathrm{U}}$ in PS2 (Fig. 8(c)) are essentially the same as in PS1 though they are less significant. On the other hand, the anomalies for $Q_{\mathrm{OA}}^{\mathrm{U}}$ in PS2 (Fig. 8(d)) reveal a substantial difference from those in PS1. While the pattern resembles Fig. 8(c) to the south of Greenland and in the subtropics, it has a large positive anomaly around 40°N, 60°W, which is not found in other composite maps. It corresponds to the sensible- and latent-heat release (mostly the latter) from the ocean associated with positive forcing SST anomalies shown in Fig. 6(b). It should be noted that in the coupled system (i.e. CTL) this heat release works not only to force the atmosphere but also to damp the positive SST anomalies themselves. The former action can produce a non-local atmospheric response, and it in turn reinforces the SST anomalies forming a large-scale positive feedback loop, as examined in detail in the rest of this paper. The CSVD analysis successfully identified this signal because the prescribed SST anomalies in PS2 were not subject to the local negative feedback. In CTL, and perhaps in observations, $Q_{\mathrm{OA}}^{\mathrm{C}}$ $(= Q_{\mathrm{AO}}^{\mathrm{C}})$ is determined by a mixture of these positive feedbacks and the one-way atmospheric forcing.

There is no doubt that the positive phase of the NAO (Figs. 4(c) and 6(a)) produces the net heat flux anomalies as shown in Fig. 8(a)–(c). At the same time, the circulation anomaly leads to a northward shift in the water-vapour transport (Hurrell 1995), which results in greater precipitation to the east of negative pressure anomalies and less

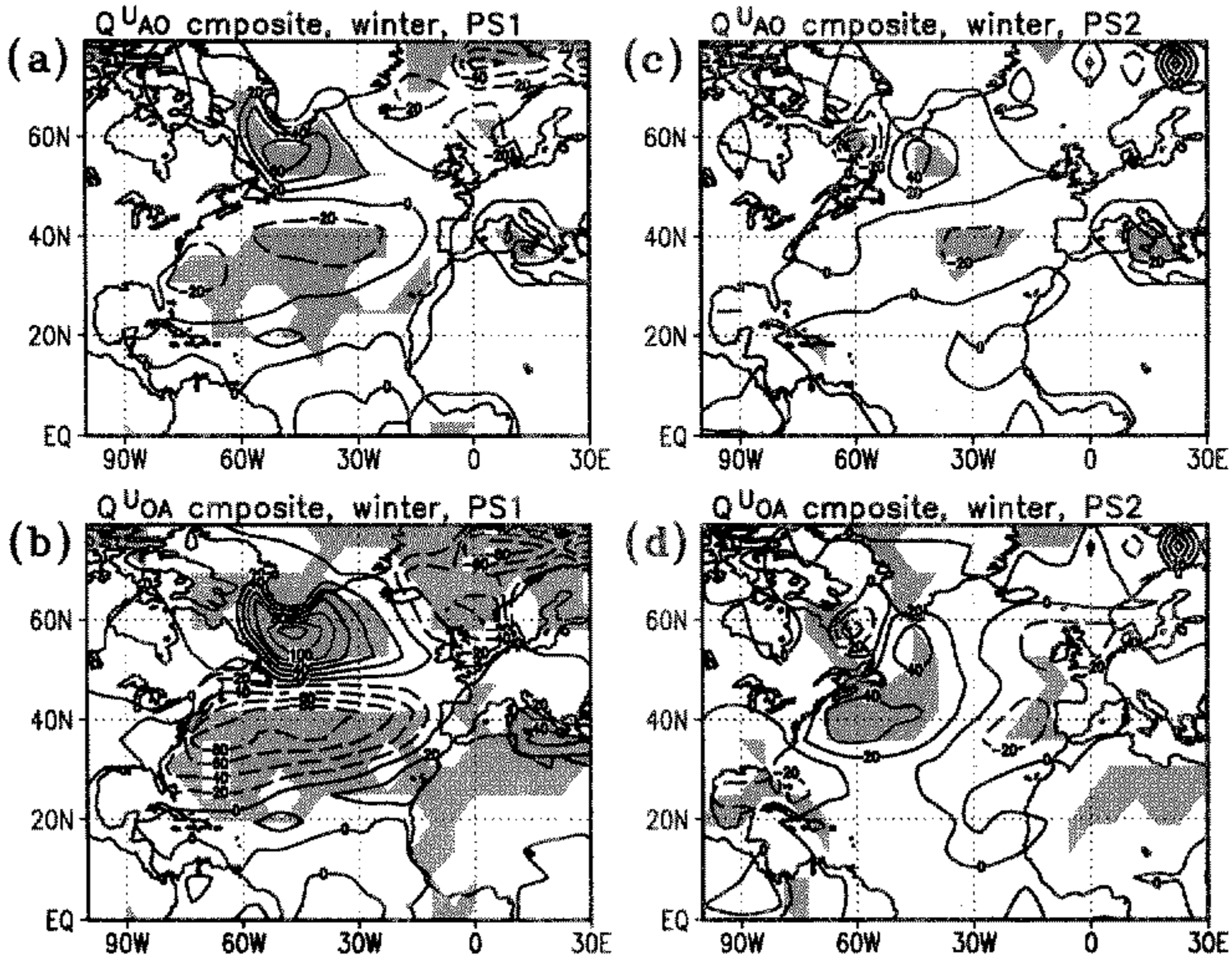

Figure 8. (a) Composite map for the uncoupled atmosphere–ocean net surface heat flux (Q^{U}_{AO}) in the winter uncoupled experiment PS1 fields, based on the sea surface temperature (SST) expansion coefficient of the leading singular value decomposition (SVD) mode (Fig. 4(c)). Shown is the difference of the positive minus negative winters, each of which consists of about ten cases. Contour interval is 20 W m^{-2} while negative contours are dashed. Statistically significant areas at the 95% level are shaded. (b) As (a), but for uncoupled ocean–atmosphere net surface heat flux (Q^{U}_{OA}). (c)–(d) As (a)–(b), but for the composites in uncoupled experiment PS2, based on the SST expansion coefficient of the leading combined SVD mode (Fig. 6). All the quantities are defined positive upward. See text for details of model experiments.

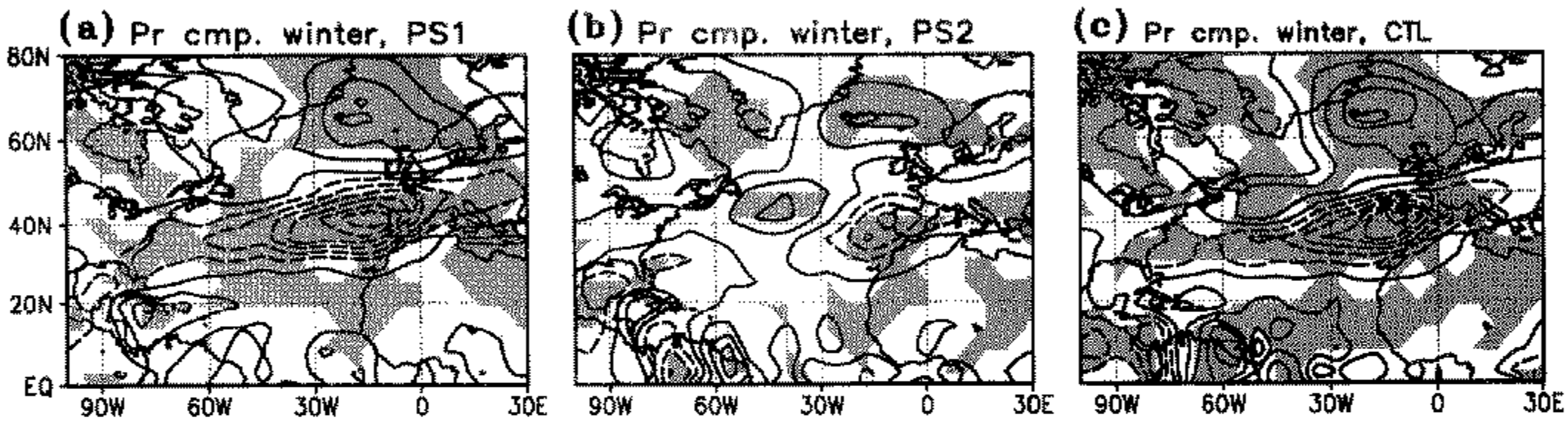

Figure 9. (a)–(b) As Fig. 8(a) and (c), respectively, but for the precipitation. (c) As Fig. 8(a), but for the precipitation composite in the winter coupled experiment CTL fields, based on the SST expansion coefficient of the leading SVD mode (Fig. 4(b)). Contour interval is 0.5 mm day^{-1}.

precipitation to the south as shown in the precipitation composite in PS1 (Fig. 9(a)). The composite shows a north–south dipole of the precipitation anomaly having an opposite sign to the height fields. In the composite precipitation map in PS2 (Fig. 9(b)), another significant anomaly is found in addition to the dipole associated with the NAO, an elliptic positive anomaly just over the centre of positive forcing SST anomalies in

Fig. 6(b). It is interesting to note that a similar positive precipitation anomaly is also found in the composite map in CTL (Fig. 9(c)). The coincidence in the locations of positive forcing SST, Q_{OA}^{U}, and precipitation anomalies indicates that the increased evaporation due to sea surface warming is locally washed out. This locally consumed water vapour is also found in a simulation by Rodwell *et al.* (1999). In the next section, the role played by the diabatic heating associated with this precipitation anomaly is examined.

5. Positive feedback loop

In this section, processes in the positive feedback mentioned in the previous section are examined in detail using two kinds of idealized experiments. One is the conventional ensemble simulation using an AGCM with and without a specified SST anomaly pattern, while another kind of experiment involves analyses using linear dynamical models.

(*a*) *Sensitivity experiment*

Two nine-member ensemble integrations are conducted using the AGCM with the same resolution as CTL: one with monthly observed climatological SSTs globally, and another with the same SSTs except over the North Atlantic where the positive SST anomaly pattern as shown in Fig. 10(a) is added. The SST anomaly pattern is derived from Fig. 6(b) with the magnitude corresponding to 3 SD (maximum of about 0.8 K); this amplitude is still smaller than that given in previous studies. Each member consists of a 10-year integration including the seasonal cycle to avoid an error in the background flow for a perpetual condition (Peng *et al.* 1997). As in PS1 and PS2, passive SST response in the slab ocean forced by the AGCM was also computed.

Shown in Fig. 10 are the equilibrium responses for the net heat flux (i.e. Q_{OA}^{U}), precipitation, mean-sea-level pressure (m.s.l.p), Z500, and SST fields. They are the differences in ensemble 10-year averages between the anomaly and climatology integrations. As expected from results presented in section 4(d), the positive SST forcing (Fig. 10(a)) induces positive flux anomalies (Fig. 10(b)) mainly due to increased evaporation, and they are converted to an *in situ* precipitation anomaly around 40°N, 45°W (Fig. 10(c)) accompanying an anomalous diabatic heating. This diabatic heating is concentrated in the lower troposphere (cf. Fig. 11(c) below). Although the m.s.l.p. response is not significant over the ocean (Fig. 10(d)), the Z500 response shows a significant dipole pattern which well resembles the NAO (Fig. 10(e)). These atmospheric responses in turn force the ocean, such that positive (negative) SST anomalies are generated in middle latitudes (south of Greenland), as shown in Fig. 10(f). The amplitude of the SST response has a maximum of 0.4 K, which is approximately half the forcing SST anomaly in Fig. 10(a).

In a hypothesis recently proposed by Peng and Whitaker (1999) for the atmospheric response to mid-latitude SST anomalies, it is mentioned that the diabatic heating due to anomalous sensible fluxes during the *initial period* of integration is of importance because the air–sea temperature difference is a maximum at this period. It appears consistent with their argument that the atmospheric responses shown in Fig. 10 are significant but quite weak because the atmosphere virtually adjusted to the SST anomalies at the equilibrium. On the other hand, the relationship between the forcing SST and atmospheric responses as extracted by the CSVD analysis does not represent the equilibrium signal but indicates slow (i.e. interannual to decadal) transient components. Thus the large diabatic heating during the initial period in AGCM experiments is reinterpreted in coupled GCM experiments, and probably also in the real coupled system, as a heating due to *local atmospheric adjustment on slow time-scales*. Furthermore, the condensation

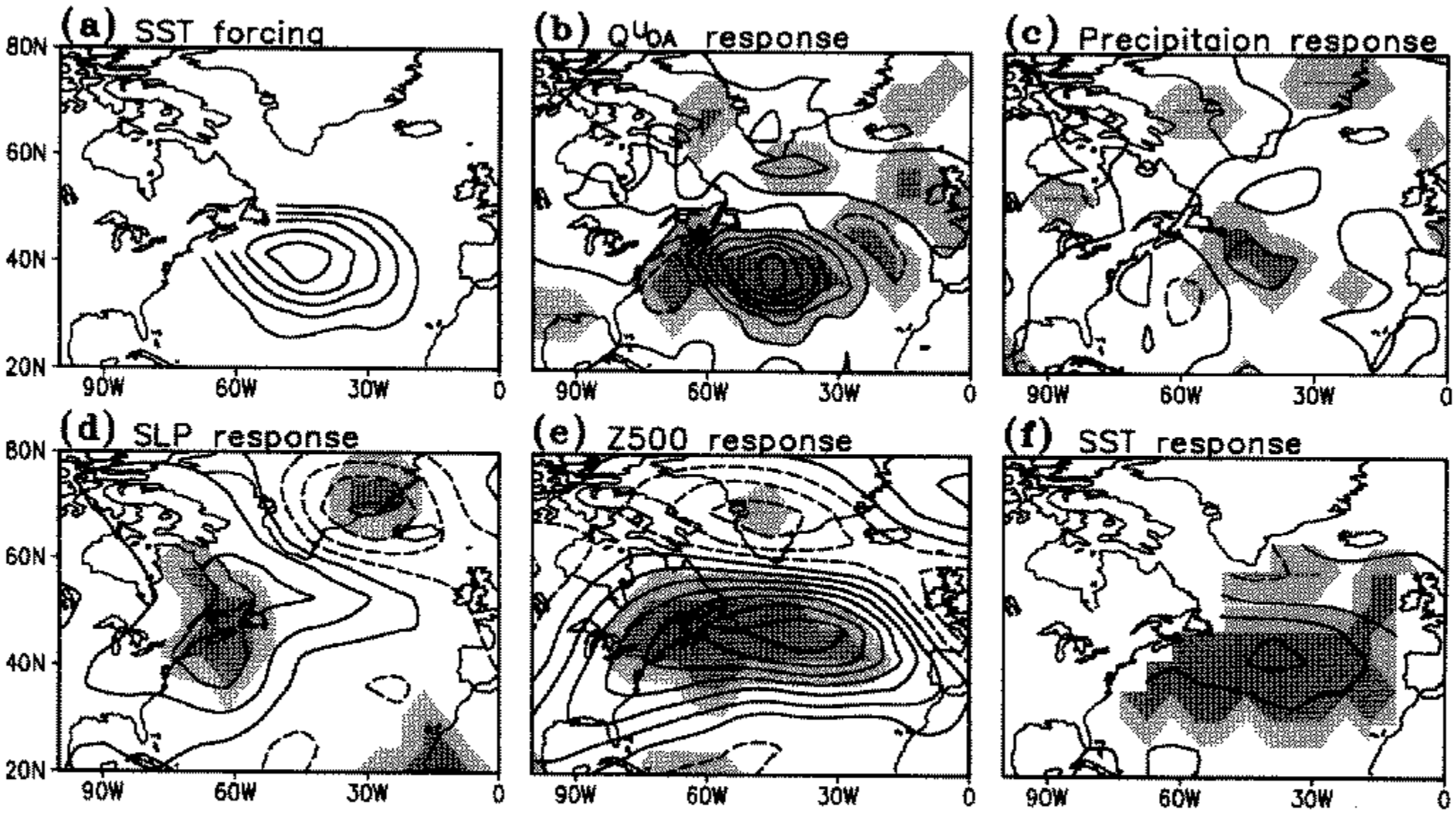

Figure 10. (a) Sea surface temperature (SST) anomalies given to nine-member ensemble experiments of the atmospheric general circulation model. Contour interval is 0.2 K. (b)–(f) Equilibrium responses to the SST anomaly pattern in (a) of the net upward fluxes of heat, precipitation, mean-sea-level pressure, 500 hPa height, and SST, with contour intervals are 1 W m^{-2}, 0.1 mm day^{-1}, 0.1 hPa, 1 m, and 0.2 K, respectively. Statistically significant areas at the 90 (95)% level are indicated by light (dark) shading.

heating seems more important than the sensible heating. The dynamics between the heating in the central North Atlantic and the NAO-like response in Z500 anomalies will be made clear in the next section.

(*b*) *Linear model experiments*

After Hoskins and Karoly (1981), numerous studies have examined the atmospheric response to a diabatic heating associated with El Niño in the equatorial Pacific, by solving steady linear equations with a given basic state and a thermal forcing (e.g. Held *et al.* 1989). Peng and Whitaker (1999) applied this technique to the question of the atmospheric response to mid-latitude SST anomalies. Calculating the steady linear response is also useful to provide an answer to the present question how the heating in the central North Atlantic excites the positive NAO.

The linear model used here is based on primitive equations identical to those in the CCSR/NIES AGCM, except for the reduction in vertical resolution from eleven to five levels (see appendix B for detail). With a basic state, $\overline{\mathbf{X}}$, derived from the winter climatology in CTL, a steady response $\mathbf{X}$ follows an equation with the matrix form

$$\mathbf{L}(\overline{\mathbf{X}})\mathbf{X} = \mathbf{F}, \tag{2}$$

where $\mathbf{F}$ indicates a forcing vector, and $\mathbf{L}$ the linear dynamical operator that consists of the right-hand-sides of Eqs. (B.1)–(B.4), respectively.

The forcing considered here is the diabatic heating associated with the positive Q^{U}_{OA} anomalies in Fig. 8(d), which is divided into two components: the anomalous sensible heating and condensation heating due to precipitation anomalies (cf. Fig. 9(b)). The former is found upstream and accounts for less than one third of the total Q^{U}_{OA} anomalies (not shown). The sensible heating is limited to within the planetary boundary layer, while the condensation heating is concentrated in the lower troposphere above

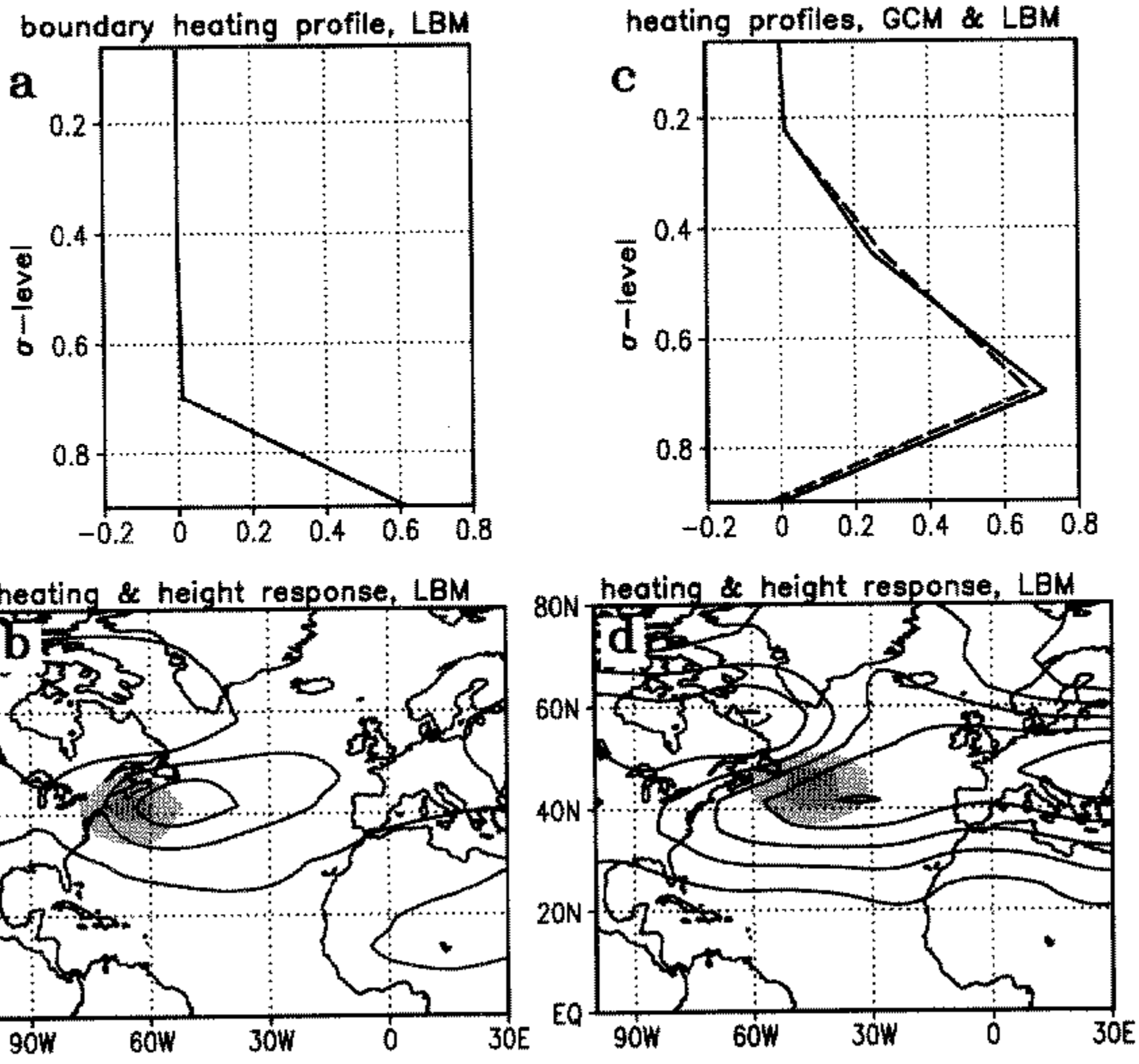

Figure 11. (a) Idealized heating profile averaged over 50°–80°W, 35°–50°N which represents the sensible heating. The horizontal axis denotes the heating rate in K day^{-1}. (b) Steady height response at 500 hPa to the sensible heating with the profile in (a). The contour intervals are 3 m; the negative contour is dashed. The heating pattern is shown for $\sigma = 0.9$ and the area with magnitude greater than 0.5 (1.0) K day^{-1} is light (dark) shaded. (c) As (a) but for the heating profile over 30°–60°W, 35°–50°N which represents the precipitation heating. The profile obtained by the composite in uncoupled experiment PS2 is shown by the dashed line. (d) As (b) but for the height response to the precipitation heating. The heating pattern is shown for $\sigma = 0.7$.

the boundary layer as confirmed by the vertical profile of the heating composite in PS2. Thus two idealized heating patterns having different profiles, as shown in Fig. 11(a) and (c), are used in Eq. (2) to obtain the direct response to the heating. The steady height responses shown in Fig. 11(b) and (d) represent large-scale, downstream positive anomalies. The response to the precipitation heating (Fig. 11(d)) has larger values and stronger projections onto the southern part of the NAO (e.g. Fig. 6(a)), suggesting a more dominant role of the latent heating than of the sensible heating.

While the sum of these atmospheric responses somewhat resembles the NAO, the negative response in high latitudes is weak and, furthermore, it contains large baroclinic components unlike equivalent barotropic anomalies of the NAO. An interaction with transient eddies is a possible candidate for converting the thermally forced, baroclinic anomalies to equivalent barotropic anomalies. In fact, Peng and Whitaker (1999) show that an interaction between the large-scale anomalies and the high-frequency, transient eddy activity is crucial in determining the atmospheric response found in their GCM. The change in transient eddies, or the storm track, in response to the presence of large-scale anomalies is evaluated by Branstator (1995) using a so-called storm track model. His work shows that the transient eddy statistics can be parametrized by a large number of linear model integrations with spatially random initial perturbations. By employing his method, we also reproduced the transient eddy statistics, defined here as

2–8 day band-passed components, using our linear model as detailed in appendix C. The interplay between large-scale anomalies and storm tracks is examined by a successive use of the steady linear model and the storm track model as follows. When we rewrite Eq. (2) as

$$\mathbf{L}(\overline{\mathbf{X}})\mathbf{X}_1 = \mathbf{Q}, \tag{3}$$

where $\mathbf{Q}$ denotes the combined sensible and latent heating shown in Fig. 11(a) and (c) while $\mathbf{X}_1$ is the thermally forced response. The eddy statistics in association with the response $\mathbf{X}_1$ are obtained by the storm track model

$$\frac{\mathrm{d}\mathbf{X}_1'}{\mathrm{d}t} + \mathbf{L}(\overline{\mathbf{X}} + \mathbf{X}_1)\mathbf{X}_1' = 0. \tag{4}$$

The anomalous eddy forcing $\mathbf{F}(\mathbf{X}_1')$, which consists of the convergence of eddy heat and vorticity fluxes, is computed by subtracting the eddy statistics under the basic state $\overline{\mathbf{X}}$ from those simulated with Eq. (4). When the eddy vorticity flux only is taken into account in $\mathbf{F}(\mathbf{X}_1')$ results were essentially the same, except for the enhancement of the response. This implies the secondary role of the eddy heat flux convergence, consistent with earlier studies showing that eddy heat fluxes are less important in the upper troposphere (Lau and Holopainen 1984) and may even be parametrized by a harmonic temperature diffusion (cf. Ting and Lau 1993). Then the steady linear model is again used to yield an eddy-induced secondary response, $\mathbf{X}_2$,

$$\mathbf{L}(\overline{\mathbf{X}} + \mathbf{X}_1)\mathbf{X}_2 = \mathbf{F}(\mathbf{X}_1'). \tag{5}$$

Figure 12 shows $\mathbf{X}_1$, $\mathbf{X}_1'$, and $\mathbf{X}_2$ obtained from the above analysis. The height response corresponding to $\mathbf{X}_1$ (Fig. 12(a)) is equal to the sum of Fig. 12(b) and (d) while $\mathbf{X}_1'$ is represented by the root-mean-square (r.m.s.) of eddy height in Fig. 12(b). In association with this large-scale pattern, changes in the transient eddy activity as simulated by the storm track model are characterized by a north–south dipole straddling the mean position of the storm track (Fig. 12(b)). While the northward deflection of the Atlantic storm track is so far found in relation to the eastern Atlantic pattern (Lau 1988), composites for band-pass eddy height with respect to the positive and negative phases of the NAO also show similar displacement in the storm track both in the GCM and the storm track model (Fig. C.2), and even in observations (e.g. Bresch and Davies 2000, their Fig. 12). The steady height response, $\mathbf{X}_2$, to the eddy vorticity and heat forcings is shown in Fig. 12(c). The pattern is a north–south dipole having a large projection onto the positive phase of the NAO. Thus the combined linear diagnostics of Eqs. (3)–(5) indicate interactions between the heating-induced anomalies and the storm track, working co-operatively to excite the NAO-like height anomalies.

It is worth examining which component in large-scale anomalies shown in Fig. 12(a) leads to the northward displacement of the storm track. For this purpose, $\mathbf{X}_1$ is divided into barotropic and baroclinic components and $\mathbf{X}_1'$ and $\mathbf{X}_2$ re-calculated for the respective components. The barotropic component is defined as the vertical average of $\mathbf{X}_1$, while the baroclinic component is the residual. The m.s.l.p. anomalies for the barotropic component are determined as they satisfy the geostrophic balance. The r.m.s. of transient eddy height associated with the barotropic, and that associated with the baroclinic, components of $\mathbf{X}_1$ show the northward deflection and north-eastward extension of the storm track, respectively (Fig. 13(a) and (c)). The northward deflection in response to the barotropic anomalies (Fig. 13(a)) is due to the steering effect by the strengthened (weakened) westerlies over the north (south) of the mean storm track, consistent with

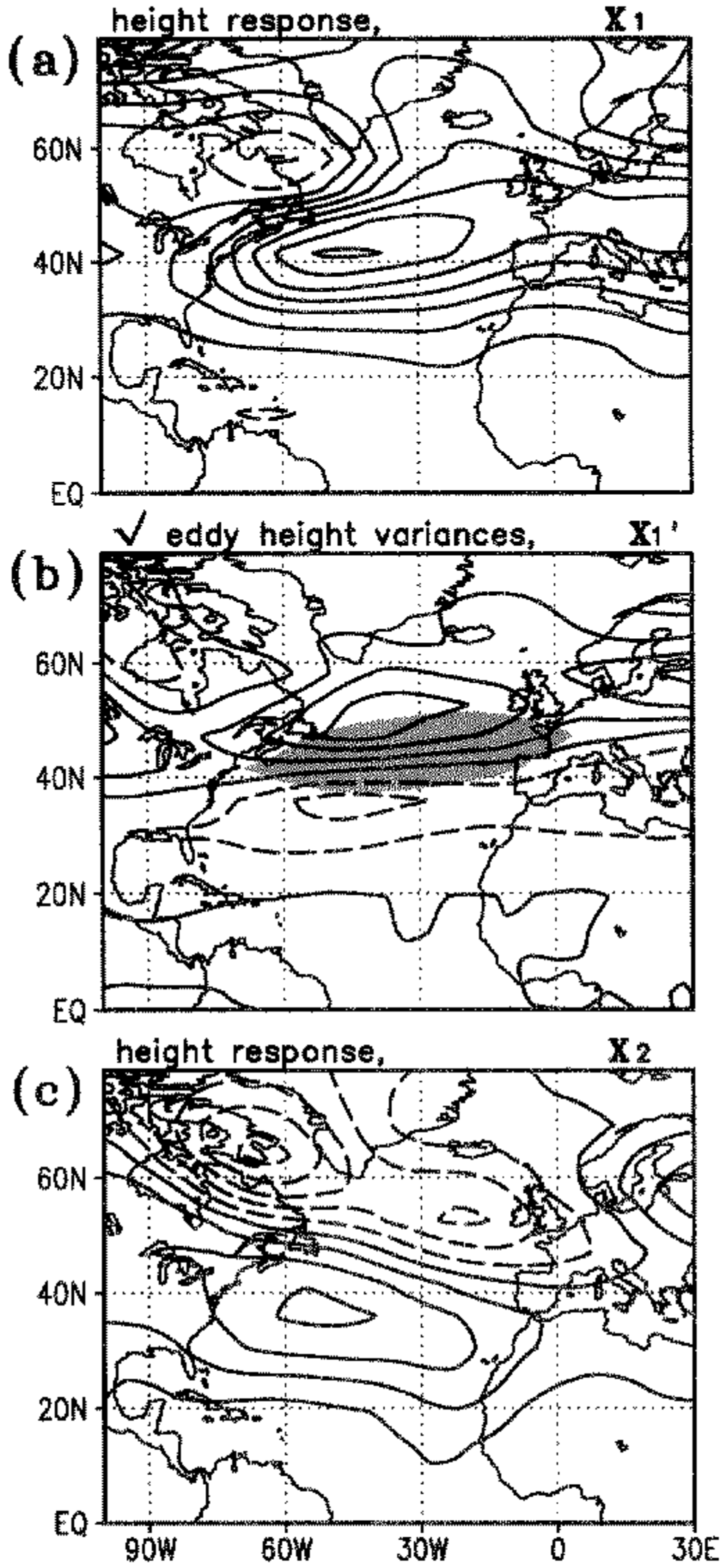

Figure 12. (a) Steady height response to the combined heating due to sensible flux and condensation, which is equal to the sum of Fig. 11(b) and (d). Contour interval is 3 m; negative contours are dashed. (b) Anomalies in the root-mean-square of the eddy height, $\sqrt{Z'^2}$, at sigma level 0.35, simulated by the storm track model. The contour interval is 1 m; shading denotes areas of the $\sqrt{Z'^2}$ climatology greater than 60 m. (c) 500 hPa height response to the eddy forcing due to convergence of eddy vorticity and heat fluxes, associated with (b). The contour interval is 1 m and negative contours are dashed.

Branstator's (1995) results. On the other hand, the north-eastward extension of the eddy activity in the baroclinic case (Fig. 13(c)) is explained not only by the increased vertical shear around 50°N but also by the reduction in the low-level thermal stability over the positive height response shown in Fig. 12(a). While both of the steady height responses to these eddy anomalies show a meridional dipole (Fig. 13(b) and (d)), the dipole response in the baroclinic case is found south-eastward of that in the barotropic case. Note that the latter pattern is very similar to the NAO, although the former is slightly dominant in magnitude. The combined linear model computation employed here (Eqs. (3)–(5)) is regarded as an approximation to the nonlinearly equilibrated interplay between

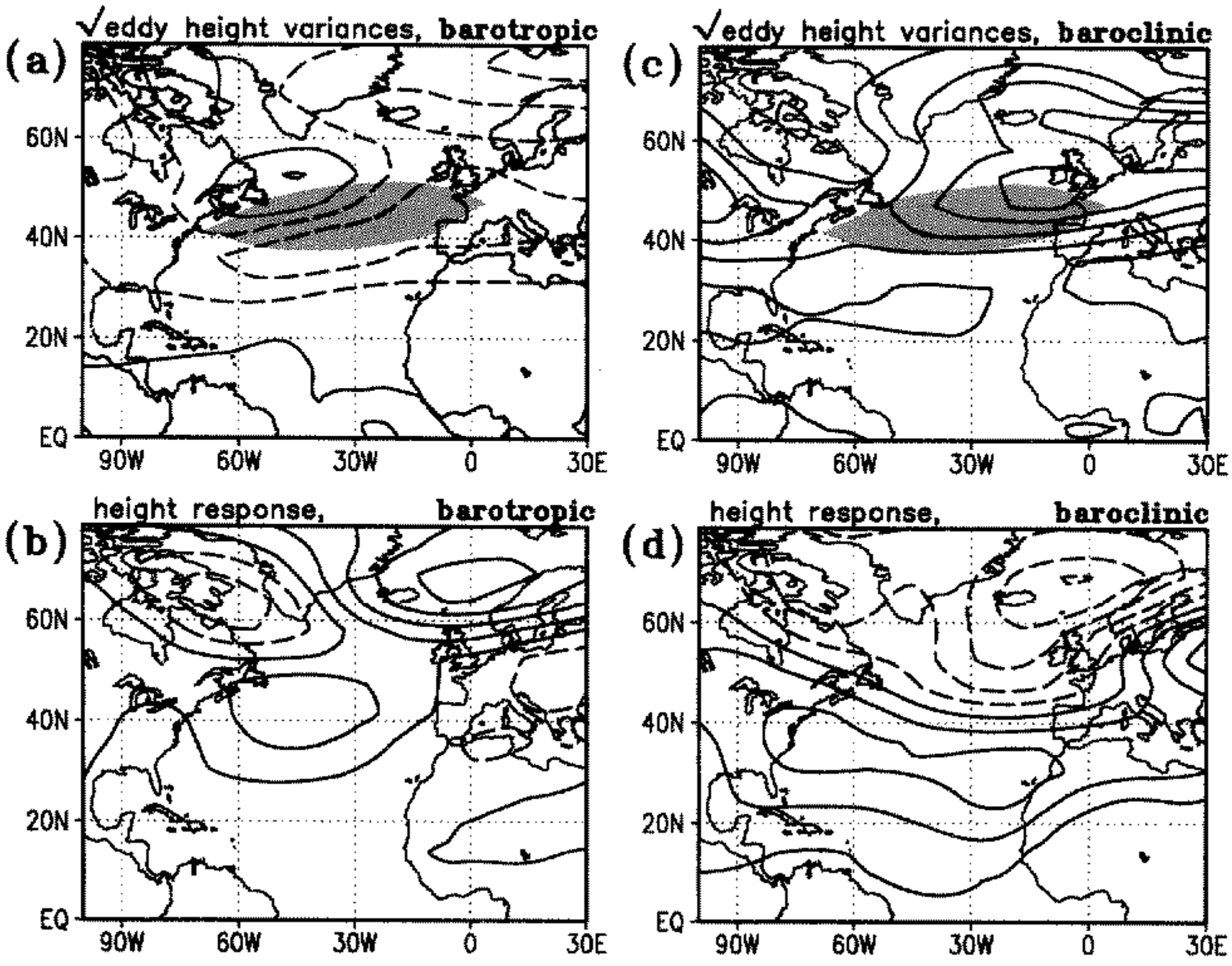

Figure 13. (a)–(b) As Fig. 12(b) and (c), but for the barotropic components of the thermally forced response, $\mathbf{X}_1$, given to the storm track model. (c)–(d) As (a)–(b), but for the baroclinic components.

quasi-stationary large-scale pattern and transient eddies. Since the eddy-induced response (Fig. 12(c)) has less baroclinic components than the heating-induced response (Fig. 12(a)), the interaction of the barotropic anomalies and storm track (Fig. 13(a) and (b)) is expected to become more important when Eqs. (3)–(5) are further iterated. Such an iteration, however, is not conducted because it is subject to increasing error due to linear approximation.

6. Summary and discussion

In this study, we have addressed the question whether a positive feedback operates between large-scale patterns in the atmosphere–ocean system over the mid-latitude North Atlantic. In order to examine the two-way interaction, 60-year integrations were conducted using a coupled GCM with and without thermal coupling. In the coupled runs, the two-way coupling is divided into the SST driving of the atmosphere and the atmospheric driving of another SST. A comparison of geopotential height and SST anomalies between the coupled and uncoupled experiments confirmed the enhancement of the atmosphere–ocean variances due to thermal coupling, as has been reported in the previous studies (Manabe and Stouffer 1996; Bladé 1997; Barsugli and Battisti 1998; Saravanan 1998; Bhatt *et al.* 1998). The effect has been explained by Barsugli and Battisti (1998) as an atmosphere–ocean *local* adjustment due to coupling, which leads to reduction in the damping heat fluxes. However, this effect brings a change to the strength of the negative feedback but does not necessarily imply a positive feedback.

A dominant set of coupled patterns simulated in the North Atlantic is characterized by tripole SST anomalies and the NAO-like dipole height anomalies, both of which are

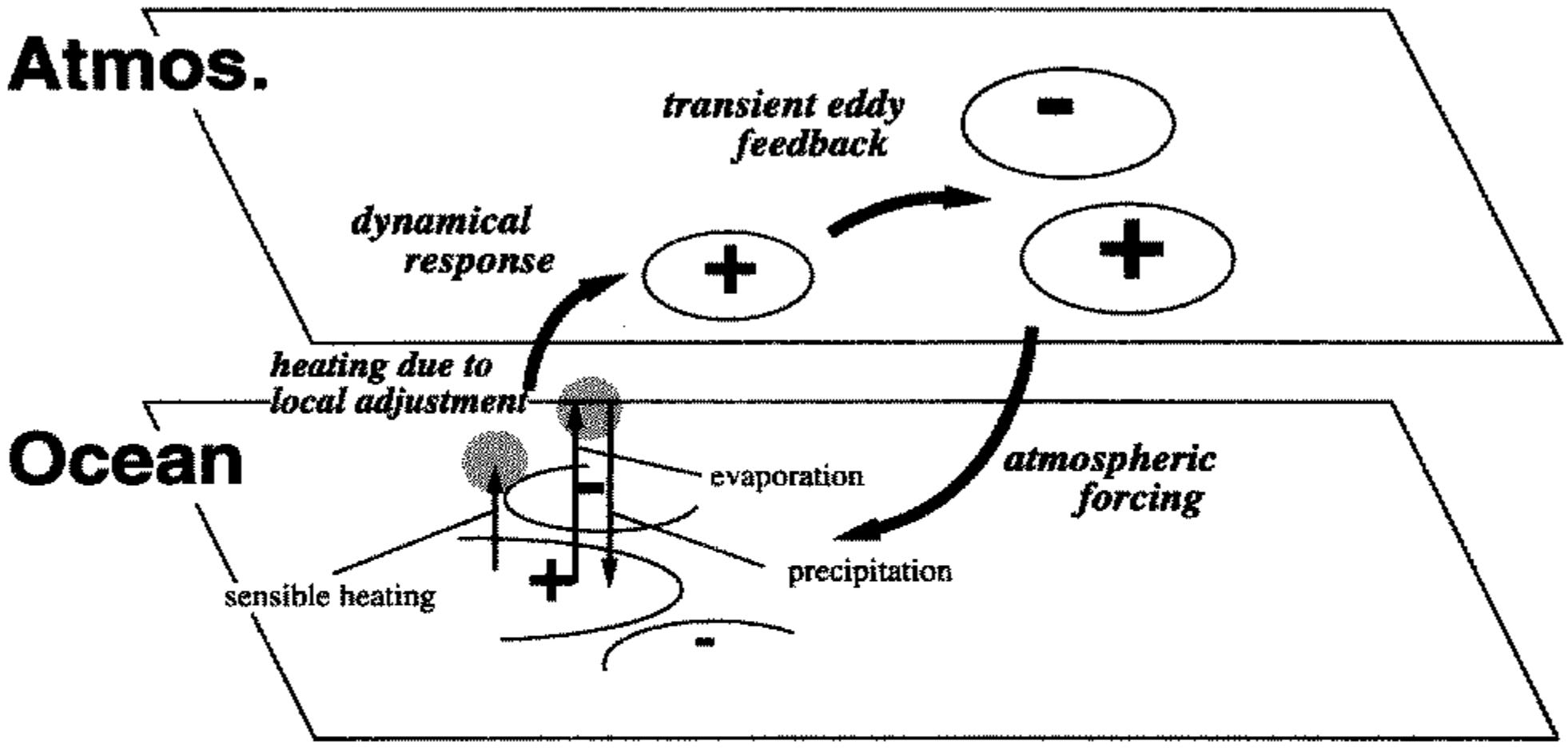

Figure 14. Schematic showing the positive feedback loop between the NAO-like anomalies and the tripole SST anomaly pattern; see text for details and description.

less sensitive to the thermal coupling (Fig. 4). On the other hand, one uncoupled case adopting prescribed SSTs derived from the coupled run (PS2) shows temporal coherence of SST and Z500 with those in the coupled run (CTL) greater than that of another uncoupled case with CTL (Fig. 5). A combined analysis of forcing (i.e. prescribed) SST, Z500, and response SST anomalies in PS2 hints that the positive forcing SST anomalies in the mid-latitude band around 40°N effectively excite the positive phase of the NAO, which in turn generates the tripole SST anomalies (Fig. 6). Since the forcing and response SST anomaly patterns in this analysis resemble each other, this suggests a *non-local* positive feedback at work in CTL. Physical processes in the feedback were examined by using composites for surface flux and precipitation fields in the GCM (cf. section 4(d)), and further by experiments with linear baroclinic models in section 5. The positive feedback loop found in these analyses is illustrated schematically in Fig. 14.

The tripole SST anomaly pattern with the polarity shown in Fig. 14 is primarily driven by the one-way atmospheric forcing associated with the positive phase of the NAO, as approximated by stochastic theory (Frankignoul 1985). On the other hand, among this tripole pattern, positive SST anomalies in the mid-latitude band induce a local atmospheric adjustment, anomalous heat being released by the ocean on a slow time-scale due to larger thermal inertia in the upper ocean. While it works to damp the SST anomalies, the large-scale atmospheric response is at the same time excited by the sensible- and condensation-heating anomalies. The large-scale anomalies having a projection on to the southern part of the NAO are further modified to the NAO-like dipole primarily due to the eddy vorticity feedback. The NAO in turn reinforces the tripole SST anomalies. This positive feedback is so weak behind the dominant atmospheric driving that it can hardly be identified from observational analyses. Nevertheless, the weak feedback could be important since it yields significant decadal peaks in a SST spectrum by combining with the ocean dynamics (Marshall *et al.* 2000; Watanabe and Kimoto 2000).

As mentioned in section 4(c), the pattern of effective SST anomalies identified by the combined SVD analysis (Fig. 6(b)) is quite similar to the SST anomaly pattern given in Palmer and Sun's (1985) AGCM study, in which the location of the SST anomalies is referred to as the RM area following an observational study by Ratcliffe and Murray (1970). They foresaw, and discussed, the importance of the diabatic heating and

the transient eddy feedback theoretically. The description of the atmospheric response induced by SST anomalies illustrated in Fig. 14 is also similar to that given by Peng and Whitaker (1999), although they focused on the North Pacific. Our analyses, however, have shown that the lower-tropospheric heating associated with precipitation anomalies is of importance to the direct response, while only the role of sensible heating in the boundary layer was discussed by Peng and Whitaker. Relative contributions of the sensible- and latent-heat anomalies to the nature of atmospheric response to SST forcing should be elaborated in the future.

Using the storm track model and anomaly fields associated with the NAO, we have confirmed that the positive phase of the NAO deflects the storm track northward (Fig. C.2), and the anomalous storm track reinforces the NAO pattern (not shown). Branstator (1995) has also shown the positive feedback between low-frequency anomaly patterns and transient eddies in a GCM. Considering these results, we can expect that the heating-induced large-scale response (Fig. 12(a)), having a large projection on the NAO, leads to the positive eddy feedback. On the other hand, it is also shown by Branstator (1995) that eddy feedback does not always reinforce the large-scale anomalies which induced it. Actually, enhancement by the eddy vorticity feedback presented in section 5(b) is sensitive to a slight change (e.g. 5 degrees) in the heating latitude, hence slight change in $\mathbf{X}_1$. Processes for the natural selection of large-scale patterns by the interaction with transient eddies should be elucidated in the dynamical perspective (e.g. Itoh and Kimoto 1999).

Coupled patterns in the GCM apparently indicate the influence of simulated NAOs on the tripole SST anomalies (Fig. 4). On the other hand, the observational counterpart in Z500 anomalies is less similar to the NAO, although the observed and modelled NAO patterns resemble each other. Since the coupled GCM employs a simple slab ocean, this difference might be attributed to the lack of ocean dynamics in the GCM experiments. It is not clear at the present stage how ocean dynamics influence the coupled atmospheric pattern, and the question should be addressed in the forthcoming studies. The coupled SST patterns also show a difference between observations and the model, such that the former has positive SST anomalies in the mid-latitude band limited to the western basin. Thus the effective SST forcing identified by the CSVD analysis (Fig. 6(b)) may be located slightly westward in the real atmosphere–ocean system. In fact, the precipitation in the NCEP re-analysis composited as in Fig. 9 reveals a positive anomaly in the central North Atlantic (not shown) but further west than that in Fig. 9(c) by about 10 degrees. An ensemble AGCM study by Venzke *et al.* (1999) could avoid this problem because they used observed SSTs as a boundary condition, although the effective SST forcing pattern and the role of transient eddy feedback have not been identified in their study. Nevertheless, both their experiment and ours consistently suggest positive air–sea feedback at work over the Atlantic. It may be useful to conduct a multi-decadal simulation like PS2 but with a higher resolution AGCM forced by observed SSTs and with a passive ocean GCM.

Consistent with Rodwell *et al.* (1999), the temporal coherence between CTL and PS2 indicates that the predictability for the atmosphere is extended with known SSTs in the North Atlantic. However, this does not imply that the predictability for the coupled system is also extended, because SSTs in the coupled system are easily disturbed by unpredictable atmospheric noise (cf. Miller and Roads 1990; Bretherton and Battisti 2000). If the ocean has a preferred time-scale, such as decadal variability, we may hope that the coupled feedback proposed in this study contributes to extending the predictability for the coupled system, as suggested in a simple framework by Czaja and Marshall (2000). A recent ensemble experiment using a coupled GCM by Grötzner

et al. (1999) actually shows extended predictability in the North Atlantic on interdecadal time-scales in their model, due to a coupled atmosphere–ocean mode. Alternatively, the positive feedback may refine the seasonal-prediction skill for the coupled system, because the local thermal damping takes several months to damp a SST anomaly given at the initial time.

APPENDIX A

Change in probability density function

The combined SVD analysis presented in section 4(c) suggests that the NAO is sensitive to SST anomalies near 40°N, especially in the box from 30° to 70°W and 30° to 45°N (Fig. 6(b)). Because the centre of positive anomalies in the forcing SST is quite close to that of positive SST anomalies in the tripole response pattern (Fig. 6(c)), a positive feedback for the ocean is suggested to be at work in a band between 30° and 45°N. The extent to which the polarity of the NAO is affected by the SST anomaly in this latitude range is evaluated by plotting a probability density function (p.d.f.) of the simulated NAO in terms of the sign of SST anomalies. For that purpose, EOFs for monthly Z500 anomalies are calculated in each field. The leading EOFs in all the fields exhibit patterns nearly identical to those in Fig. 4(b)–(d). Time coefficients of these EOFs are used to define the polarity of the NAO. The results were not altered when using temporal coefficients obtained from a spatial projection of Z500 anomaly patterns shown in Fig. 4 onto monthly Z500 fields.

Shown in Fig. A.1(a) are p.d.f.s of the simulated NAO in CTL when SST anomalies in 30°–70°W, 30°–45°N exceed ±1 SD (solid and dashed lines), superimposed on a mean distribution (shading) obtained from 12 (month) ×60 (year) = 720 samples. It is obvious that the p.d.f. shifts towards positive and negative regimes when the mid-latitude SST anomalies are positive and negative, respectively. However, most of this shift reflects that the extreme phase of the NAO drives the underlying SST anomalies but not vice versa, because similar shifts in p.d.f.s are found in PS1 and PS2 in terms of signs in their *response* SST anomalies (not shown). True shift in the p.d.f. in response to the forcing due to SST anomalies is much smaller as shown in Fig. A.1(b), which displays the p.d.f.s of the NAO in PS2 in terms of the sign in the *forcing* SST anomalies. While the shift in the polarity of the NAO is too small to be significant, it produces a much more apparent shift in the p.d.f. of the tripole pattern in *response* SST anomalies (Fig. A.1(c)). Here the polarity of the tripole pattern is defined by the leading EOF of monthly response SST anomalies in PS2. A difference in the width of p.d.f.'s shift in Fig. A.1(b) and (c) is attributed to the difference in the signal-to-noise ratio between the atmosphere and the ocean. This implies that the positive feedback signal for the atmosphere is hard to detect while that for the ocean is much easily found, a remark similar to that made regarding Fig. 5.

APPENDIX B

Linear baroclinic model

The linear model used in this study is based on primitive equations identical to those used in the CCSR/NIES AGCM. Equations for vorticity (ζ), divergence (D), temperature (T), and the logarithm of surface pressure ($\ln P_s \equiv \pi$) on a vertical sigma coordinate are exactly linearized about a basic state denoted as $\overline{(\ )}$. The linearized set of

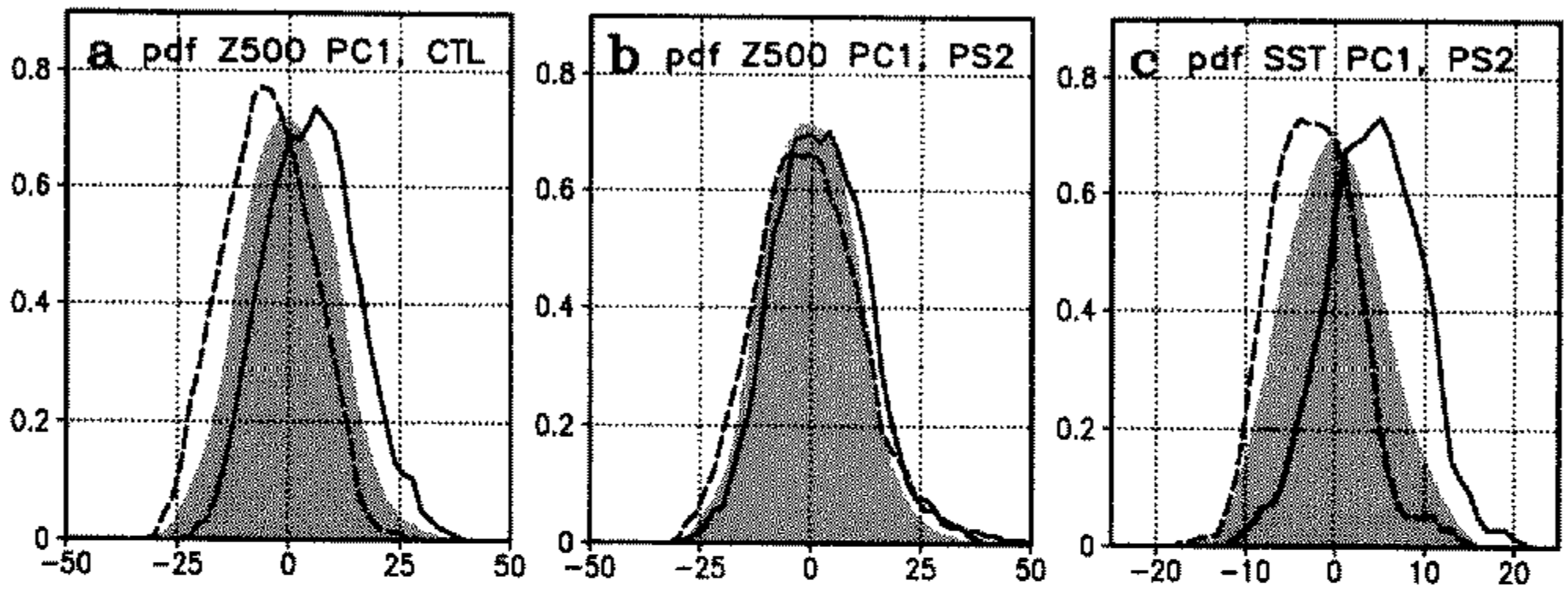

Figure A.1. (a) Probability density function (p.d.f.) for the leading empirical orthogonal function (EOF) of monthly 500 hPa height anomalies in the coupled general circulation experiment CTL, which represents the North Atlantic Oscillation. The shading indicates the mean distribution, while the solid and dashed lines denote composites in terms of the positive and negative months (greater than one standard deviation) in the time series of sea surface temperature (SST) anomalies averaged over 30°–70°W, 30°–45°N. (b) As (a) but for the p.d.f. in uncoupled experiment PS2 in terms of the forcing SST anomaly series. (c) As (b), but for the leading EOF of monthly SST anomalies in uncoupled experiment PS2, which represent a tripole similar to Fig. 4(d). See text for details of experiments.

equations for perturbations, $(\,)'$, are written as:

$$\frac{\partial \zeta'}{\partial t} = \frac{1}{a\cos\varphi}\frac{\partial A'_v}{\partial \lambda} - \frac{1}{a\cos\varphi}\frac{\partial}{\partial \varphi}(A'_u \cos\varphi) - \alpha\zeta' - K_v\left(\nabla^4 - \frac{2^2}{a^4}\right)\zeta', \tag{B.1}$$

$$\frac{\partial D'}{\partial t} = \frac{1}{a\cos\varphi}\frac{\partial A'_u}{\partial \lambda} + \frac{1}{a\cos\varphi}\frac{\partial}{\partial \varphi}(A'_v \cos\varphi) - \nabla^2_\sigma(\Phi' + R[\overline{T}]\pi' + E') - \alpha D' - K_v\left(\nabla^4 - \frac{2^2}{a^4}\right)D', \tag{B.2}$$

$$\frac{\partial T'}{\partial t} = -\frac{1}{a\cos\varphi}\frac{\partial}{\partial \lambda}\left(\overline{u}\widetilde{T}' + u'\overline{\widetilde{T}}\right) - \frac{1}{a}\frac{\partial}{\partial \varphi}(\overline{v}\widetilde{T}' + v'\overline{\widetilde{T}})\cos\varphi + \widetilde{T}'\overline{D} + \overline{\widetilde{T}}D' - \overline{\dot{\sigma}}\frac{\partial T'}{\partial \sigma} - \dot{\sigma}'\frac{\partial \overline{T}}{\partial \sigma} + \kappa T'\left(\frac{\partial \overline{\pi}}{\partial t} + \overline{\mathbf{v}}_{\mathrm{H}}\cdot\nabla_\sigma\overline{\pi} + \frac{\overline{\dot{\sigma}}}{\sigma}\right) + \kappa\overline{T}\left(\frac{\partial \pi'}{\partial t} + \mathbf{v}'_{\mathrm{H}}\cdot\nabla_\sigma\overline{\pi} + \overline{\mathbf{v}}_{\mathrm{H}}\cdot\nabla_\sigma\pi' + \frac{\dot{\sigma}'}{\sigma}\right) - \alpha T' - K_{\mathrm{h}}\left(\nabla^4 - \frac{2^2}{a^4}\right)T', \tag{B.3}$$

$$\frac{\partial \pi'}{\partial t} = -\overline{\mathbf{v}}_{\mathrm{H}}\cdot\nabla_\sigma\pi' - \mathbf{v}'_{\mathrm{H}}\cdot\nabla_\sigma\overline{\pi} - \nabla_\sigma\cdot\overline{\mathbf{v}}_{\mathrm{H}} - \nabla_\sigma\cdot\mathbf{v}'_{\mathrm{H}} - \frac{\partial\overline{\dot{\sigma}}}{\partial\sigma} - \frac{\partial\dot{\sigma}'}{\partial\sigma}, \tag{B.4}$$

where $\mathbf{v}_{\mathrm{H}}$ is the horizontal wind vector, and:

$$A'_u = \zeta'\overline{v} + (\overline{\zeta} + f)v' - \overline{\dot{\sigma}}\frac{\partial u'}{\partial\sigma} - \dot{\sigma}'\frac{\partial\overline{u}}{\partial\sigma} - \frac{R\overline{\widetilde{T}}}{a\cos\varphi}\frac{\partial\pi'}{\partial\lambda} - \frac{R\widetilde{T}'}{a\cos\varphi}\frac{\partial\overline{\pi}}{\partial\lambda}, \tag{B.5}$$

$$A'_v = -\zeta'\overline{u} + (\overline{\zeta} + f)u' - \overline{\dot{\sigma}}\frac{\partial v'}{\partial\sigma} - \dot{\sigma}'\frac{\partial\overline{v}}{\partial\sigma} - \frac{R\overline{\widetilde{T}}}{a}\frac{\partial\pi'}{\partial\varphi} - \frac{R\widetilde{T}'}{a}\frac{\partial\overline{\pi}}{\partial\varphi}, \tag{B.6}$$

$$\Phi' = -\int_1^\sigma \frac{RT'_v}{\sigma}\,\mathrm{d}\sigma, \tag{B.7}$$

$$\dot{\sigma}' = \sigma \int_0^1 \overline{\mathbf{v}}_H \cdot \nabla_\sigma \pi' \, d\sigma + \sigma \int_0^1 \mathbf{v}'_H \cdot \nabla_\sigma \overline{\pi} \, d\sigma - \int_0^\sigma \overline{\mathbf{v}}_H \cdot \nabla_\sigma \pi' \, d\sigma$$
$$- \int_0^\sigma \mathbf{v}'_H \cdot \nabla_\sigma \overline{\pi} \, d\sigma + \sigma \int_0^1 D' \, d\sigma - \int_0^\sigma D' \, d\sigma. \tag{B.8}$$

The symbol E' in Eq. (B.2) denotes the perturbation kinetic energy. In several terms of the above equations, temperature is decomposed into the global average and the deviation as $T = [T(\sigma)] + \tilde{T}$. All other symbols have the conventional meaning.

The only three differences from the dynamics in the AGCM are the following: reduction of the number of vertical levels from eleven to five due to limitation of computational resources; an introduction of Newtonian damping terms with the coefficient α; and stronger horizontal diffusion. The damping coefficient is set at 2 day^{-1} for the lowest sigma level ($\sigma = 0.90$) but at 30 day^{-1} for the upper levels. The horizontal diffusion coefficients, K_ν and K_h, are equal at 8×10^{16} m^{4}s^{-1}, which corresponds to the e-folding decay time of one day for the largest wave number.

A dynamical operator $\mathbf{L}$ as a function of the basic state is computed following Hoskins and Karoly (1981). Steady stationary responses to a forcing vector presented in section 5(b) are obtained solving Eq. (2). The linear baroclinic model as represented by the exactly linearized form has been used by Branstator (1990) and Ting and Held (1990). To obtain the stationary response to a given forcing does not necessarily require the linearization of equations (cf. Hoskins and Karoly 1981). However, such a linearized model is useful to perform a linear budget analysis (Branstator 1992) and to develop the storm track model described below.

APPENDIX C

Storm track model

A numerical model based on linear dynamics which include baroclinicity, that simulates realistic transient eddy statistics that represent the storm track activity, called the storm track model, has been developed by Branstator (1995) and Whitaker and Sardeshmukh (1998). The former simulates the eddy statistics with a large number of ensembles of the short integration with the linear primitive model, while the latter solves the eigenmodes of a linear operator for the quasi-geostrophic model to obtain the eddy covariance. The storm track model used here basically follows that of Branstator (1995).

The model consists of the same linearized primitive equations as in appendix B, except for the number of vertical levels and strength of damping. Because this model does not require a matrix inversion, unlike the steady linear model, it was possible to adopt 11, rather than five, levels. The finer vertical-resolution required the coefficient for the linear damping, α in Eqs. (B.1)–(B.3), to be set at 2 day^{-1} for the boundary layers $\sigma > 0.9$, 4 day^{-1} for levels $0.9 \geqslant \sigma > 0.8$, and zero elsewhere. The horizontal diffusion is also changed from ∇^4 to ∇^8 which is used in the GCM. The model allows natural growth of numerous modes in the linear system with a given basic state during the time integration. Eddy statistics, such as the eddy momentum flux, are computed using an ensemble of daily perturbation fields grown out of random initial perturbations. The time-integration approach avoids the difficulty in the eigenanalysis in obtaining the eddy statistics (see discussion by Branstator 1995). It requires instead a large number of ensembles for statistical robustness. Thus 500 integrations are performed with the same basic state and spatially random initial perturbations.

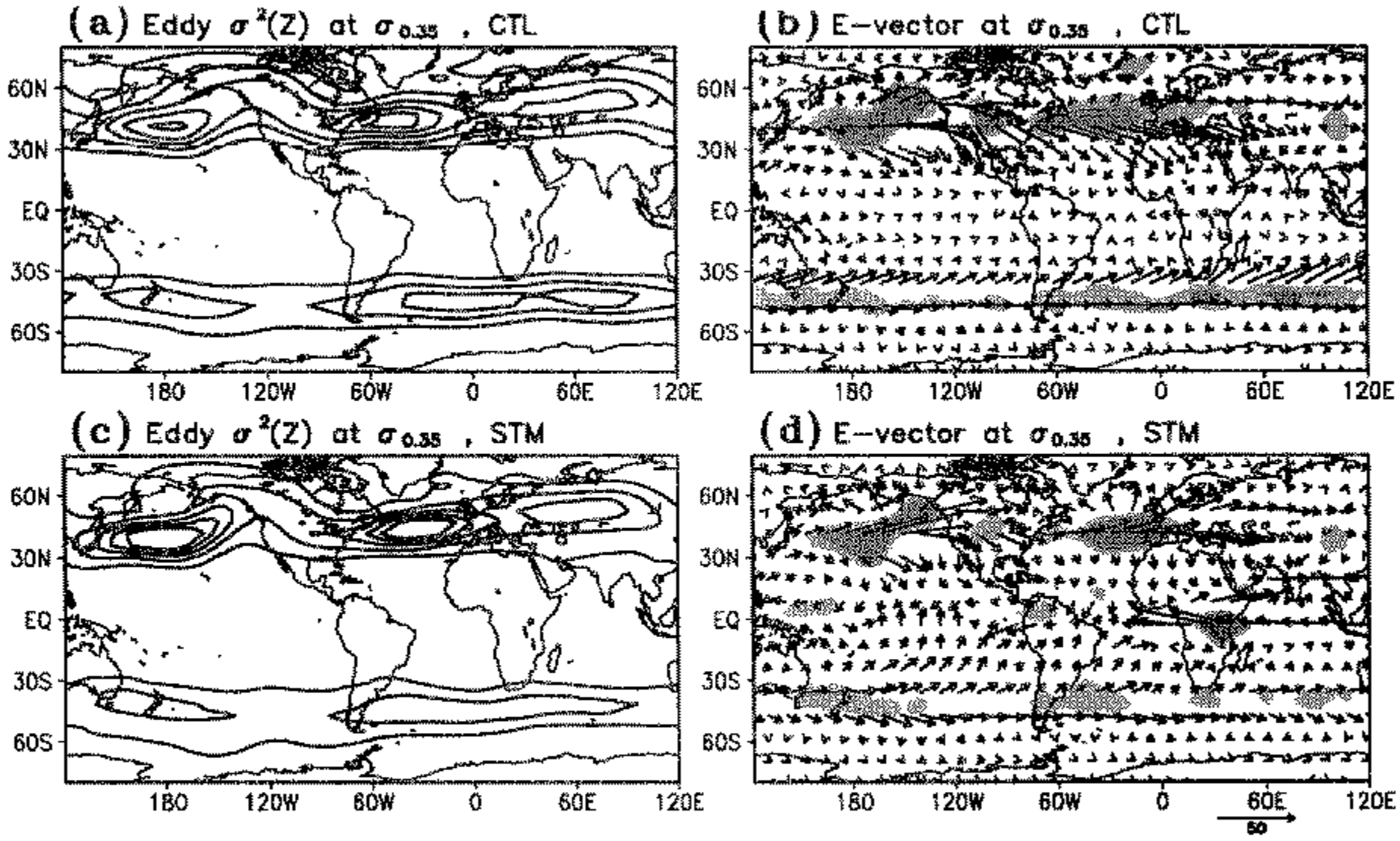

Figure C.1. (a) Winter climatology of the transient eddy height variance at $\sigma = 0.35$ in coupled general circulation experiment CTL. The contour interval is 1000 m^2. (b) As (a) but for horizontal components of the **E**-vector of Hoskins *et al.* (1983) ($m^2 s^{-2}$). The westerly accelerated regions corresponding to the **E**-vector divergence of more than 0.5 (1.0) $m\ s^{-1} day^{-1}$ are indicated by light (dark) shading. (c)–(d) As (a)–(b) but for the simulation by the storm track model. The basic state is winter climatology derived from CTL. See text for further details.

The eddy covariance fields to be simulated by the storm track model are those for 2–8 day band-pass eddies in CTL. The winter climatology of the eddy height variance, Hoskins *et al.*'s (1983) **E**-vector, and its divergence at $\sigma = 0.35$ in CTL are shown in Fig. C.1(a) and (b). In a similar manner to observations, the eddy height variance peaks in the North Pacific and in the North Atlantic (i.e. storm track regions), and the associated momentum flux convergence tends to accelerate westerlies over the middle of the Pacific and Atlantic jets, as inferred from the **E**-vector divergence. For the eddy quantities in the model to match well the above eddy statistics in the GCM, some tuning was necessary before using the storm track model. Branstator (1995) pointed out the following three parameters for the tuning: amplitude of initial perturbations, length of time integration, and damping coefficients. The first and third parameters concern the amplitude of storm tracks, while the second affects their shape (cf. Fig. 3 of Branstator 1995). In this regard, the appropriate choice of the integration period turned out to be the most important. Since it is known that nonlinear processes are involved in the decay stage of the transient eddies, we should stop the integration before reaching a peak of eddy growth. Therefore, the last five days of a six-day integration are used for the ensemble average. The damping coefficients were set as mentioned above, and the initial perturbations were prepared with their spatial SDs for vorticity, divergence, and temperature perturbations having values 6.7×10^{-6} s^{-1}, 6.7×10^{-7} s^{-1}, and 6.7 K, respectively.

The eddy statistics obtained by the storm track model with the basic state from winter climatology in CTL are shown in Fig. C.1(c) and (d). They reproduce the characteristics of GCM eddy quantities well, except for two discrepancies: the maximum eddy height variance in the linear model has larger values in the centres of storm tracks, and the momentum flux is weaker than the GCM fields in the south of the storm tracks. The latter implies that the linear model cannot simulate the correct shape of transient eddies

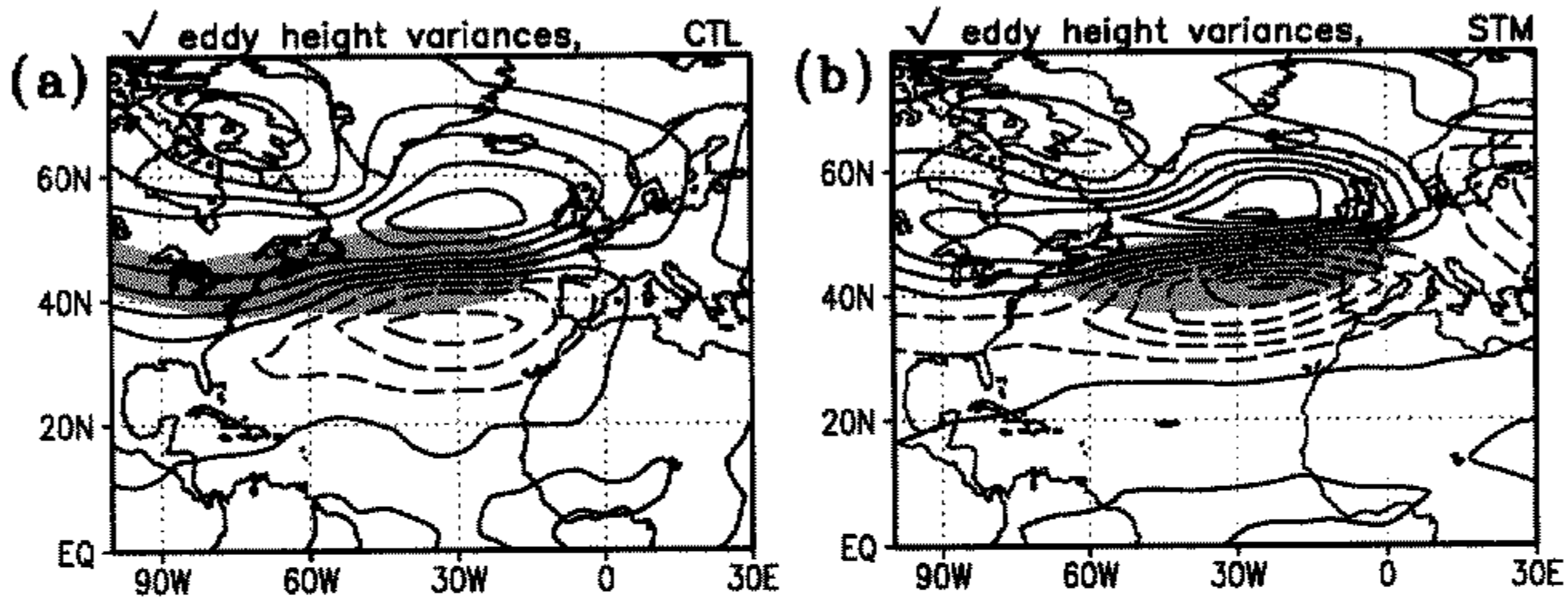

Figure C.2. (a) Composite difference in the root-mean-square of the eddy height, $\sqrt{Z'^2}$, at $\sigma = 0.35$, between the positive and negative phases of the North Atlantic Oscillation in coupled general circulation experiment CTL. The contour interval is 5 m; shading denotes areas of the $\sqrt{Z'^2}$ climatology greater than 60 m. (b) As (a) but for the simulation by the storm track model. See text for details of models.

in the GCM. Nevertheless, the E-vector divergence in the storm track model reproduced well the features (i.e. location and magnitude) in the GCM. Another example is shown in Fig. C.2 for the anomalous eddy activity associated with the NAO. Figure C.2(a) shows the composite difference of eddy height anomalies between the positive and negative phases of the NAO as defined by the leading EOF of monthly height anomalies in CTL (cf. appendix A). A northward (southward) displacement of the storm track is found in the positive (negative) phase of the NAO. On the other hand, eddy anomalies in Fig. C.2(b) are obtained from the storm track model by taking differences between the simulated fields with and without NAO anomalies in the basic state. While the linear model slightly overestimates the eddy activity as in Fig. C.1, the essential feature of the northward deflection is reproduced by the model.

ACKNOWLEDGEMENTS

The authors thank two anonymous reviewers for their useful comments. This work was supported in part by a Grant-in-Aid for Scientific Research from the Ministry of Education, Science, and Culture of Japan.

REFERENCES

Barnston, A. G. and Livezey, R. E. 1987 Classification, seasonality and persistence of low-frequency atmospheric circulation patterns. *Mon. Weather Rev.*, **115,** 1083–1126

Barsugli, J. J. and Battisti, D. S. 1998 The basic effects of atmosphere–ocean thermal coupling on midlatitude variability. *J. Atmos. Sci.*, **55,** 477–493

Bhatt, U.S., Alexander, M. A., Battisti, D. S., Houghton, D. D. and Keller, L. M. 1998 Atmosphere–ocean interaction in the North Atlantic: near surface climate variability. *J. Climate*, **11,** 1615–1632

Bjerknes, J. 1964 Atlantic air–sea interaction. *Adv. in Geophys.*, **10,** 1–82

Bladé, I. 1997 The influence of midlatitude ocean–atmosphere coupling on the low-frequency variability of a GCM. Part I: No tropical forcing. *J. Climate*, **10,** 2087–2106

Branstator, G. 1990 Low-frequency patterns induced by stationary waves. *J. Atmos. Sci.*, **47,** 629–648

1992 The maintenance of low-frequency atmospheric anomalies. *J. Atmos. Sci.*, **49,** 1924–1945

Branstator, G. 1995 Organization of storm track anomalies by recurring low-frequency circulation anomalies. *J. Atmos. Sci.*, **52,** 207–226

Bresch, D. N. and Davies, H. C. 2000 Covariation of the mid-tropospheric flow and the SST of the North Atlantic: A statistical analysis. *Theor. Appl. Climatol.*, **65,** 197–214

Bretherton, C. S. and Battisti, D. S. 2000 An interpretation of the results from atmospheric general circulation models forced by the time history of the observed sea surface temperature distribution. *Geophys. Res. Lett.*, **27,** 767–770

Bretherton, C. S., Smith, C. and Wallace, J. M. 1992 An intercomparison of methods for finding coupled patterns in climate data. *J. Climate*, **5,** 541–560

Cayan, D. R. 1992 Latent and sensible heat flux anomalies over the northern oceans: Driving the sea surface temperature. *J. Phys. Oceanogr.*, **22,** 859–881

Czaja, A. and Marshall, J. 2000 On the interpretation of AGCMs response to prescribed time-varying SST anomalies. *Geophys. Res. Lett.*, **27,** 1927–1930

Ferranti, L., Molteni, F. and Palmer, T. N. 1994 Impact of localized tropical and extratropical SST anomalies in ensembles of seasonal GCM integrations. *Q. J. R. Meteorol. Soc.*, **120,** 1613–1645

Frankignoul, C. 1985 Sea surface temperature anomalies, planetary waves, and air–sea feedback in the middle latitudes. *Rev. Geophys.*, **23,** 357–390

Grötzner, A., Latif, M., Timmerman, A. and Voss, R. 1999 Interannual to decadal predictability in a coupled ocean–atmosphere general circulation model. *J. Climate*, **12,** 2607–2624

Held, I. M., Lyons, S. W. and Nigam, S. 1989 Transients and the extratropical response to El Niño. *J. Atmos. Sci.*, **46,** 163–174

Hoskins, B. J. and Karoly, D. J. 1981 The steady linear response of a spherical atmosphere to thermal and orographical forcing. *J. Atmos. Sci.*, **38,** 1179–1196

Hoskins, B. J., James, I. N. and White, G. H. 1983 The shape, propagation and mean-flow interaction of large-scale weather systems. *J. Atmos. Sci.*, **40,** 1595–1612

Hurrell, J. W. 1995 Decadal trends in the North Atlantic oscillation: Regional temperatures and precipitation. *Science*, **269,** 676–679

Itoh, H. and Kimoto, M. 1999 Weather regimes, low-frequency oscillations, and principal patterns of variability: A perspective of extratropical low-frequency variability. *J. Atmos. Sci.*, **56,** 2684–2705

Iwasaka, N. and Wallace, J. M. 1995 Large scale air–sea interaction in the northern hemisphere from a view point of variations of surface heat flux by SVD analysis. *J. Meteorol. Soc. Jpn*, **73,** 781–794

Kushnir, Y. and Held, I. M. 1996 Equilibrium atmospheric response to North Atlantic SST anomalies. *J. Climate*, **9,** 1208–1220

Lau, N. C. 1988 Variability of the observed midlatitude storm tracks in relation to low-frequency changes in the circulation pattern. *J. Atmos. Sci.*, **45,** 2718–2743

Lau, N. C. and Holopanien, E. O. 1984 Transient eddy forcing of the time-mean flow as identified by geopotential tendencies. *J. Atmos. Sci.*, **41,** 313–328

Lau, N. C. and Nath, M. J. 1996 The role of the 'atmospheric bridge' in linking tropical Pacific ENSO events to extratropical SST anomalies. *J. Climate*, **9,** 2036–2057

Manabe, S. and Stouffer, R. J. 1996 Low-frequency variability of surface air temperature in a 1000-year integration of a coupled atmosphere–ocean–land surface model. *J. Climate*, **9,** 376–393

Marshall, J., Johnson, H. and Goodman, J. 2000 A study of the interaction of the North Atlantic Oscillation with ocean circulation. *J. Climate*, **13,** in press

Mellor, G. L. and Yamada, T. 1974 A hierarchy of turbulence closure models for the planetary boundary layer. *J. Atmos. Sci.*, **31,** 1791–1806

1982 Development of a turbulence closure model for geophysical fluid problems. *Rev. Geophys. Space Phys.*, **20,** 851–875

Miller, A. J. and Roads, J. O. 1990 A simplified coupled model of extended-range predictability. *J. Climate*, **3,** 523–542

Münnich, M., Latif, M., Venzke, S. and Maier-Reimer, E. 1998 Decadal oscillations in a simple coupled model. *J. Climate*, **11,** 3309–3319

Neelin, J. D. and Weng, W. 1999 Analytical prototypes for ocean–atmosphere interaction at midlatitudes, Part I: Coupled feedbacks as a sea surface temperature dependent stochastic process. *J. Climate*, **12,** 697–721

Numaguti, A., Takahashi, M., Nakajima, T. and Sumi, A. 1995 Development of an atmospheric general circulation model. Pp. 1–27 in *Climate system dynamics and modelling*. Ed. T. Matsuno. Center for Climate System Research, University of Tokyo. (Available from CCSR, University of Tokyo, 4–6–1 Komaba, Meguro, Tokyo 153–8904, Japan)

Palmer, T. N. and Sun, Z. 1985 A modeling and observational study of the relationship between sea surface temperatures in the north-west Atlantic and the atmospheric general circulation. *Q. J. R. Meteorol. Soc.*, **111,** 947–975

Peng, S. and Whitaker, J. S. 1999 Mechanisms determining the atmospheric response to midlatitude SST anomalies. *J. Climate*, **12,** 1393–1408

Peng, S., Mysak, L. A., Ritchie, H., Derome, J. and Dugas, B. 1995 The differences between early and midwinter atmospheric response to sea surface temperature anomalies in the northwest Atlantic. *J. Climate*, **8,** 137–157

Peng, S., Robinson, W. A. and Hoerling, M. P. 1997 The modeled atmospheric response to midlatitude SST anomalies and its dependence on background circulation states. *J. Climate*, **10,** 971–987

Ratcliffe, R. A. S. and Murray, R. 1970 New lagged associations between North Atlantic sea temperatures and European pressure, applied to long-range weather forecasting. *Q. J. R. Meteorol. Soc.*, **96,** 226–246

Rodwell, M. J., Rowell, D. P. and Folland, C. K. 1999 Oceanic forcing of the wintertime North Atlantic Oscillation and European climate. *Nature*, **398,** 320–323

Saravanan, R. 1998 Atmospheric low-frequency variability and its relationship to midlatitude SST variability: Studies using the NCAR Climate System Model. *J. Climate*, **11,** 1386–1404

Shen, X., Kimoto, M. and Sumi, A. 1998 Role of land surface processes associated with interannual variability of broad-scale Asian summer monsoon as simulated by the CCSR/NIES AGCM. *J. Meteorol. Soc. Jpn.*, **76,** 217–236

Ting, M. and Held, I. M. 1990 The stationary wave response to a tropical SST anomaly in an idealized GCM. *J. Atmos. Sci.*, **47,** 2546–2566

Ting, M. and Lau, N. C. 1993 A diagnostic and modeling study of the monthly mean wintertime anomalies appearing in a 100-year GCM experiment. *J. Atmos. Sci.*, **50,** 2845–2867

Venzke, S., Allen, M. R., Sutton, R. T. and Rowell, D. P. 1999 The atmospheric response over the North Atlantic to decadal changes in sea surface temperature. *J. Climate*, **12,** 2562–2584

Wallace, J. M., Smith, C. and Jiang, Q. 1990 Spatial patterns of atmosphere–ocean interaction in the northern winter. *J. Climate*, **3,** 990–998

Wallace, J. M., Smith, C. and Bretherton, C. S. 1992 Singular value decomposition of wintertime sea surface temperature and 500 mb height anomalies. *J. Climate*, **5,** 561–576

Watanabe, M. and Kimoto, M. 2000 Behavior of midlatitude decadal oscillations in a simple atmosphere–ocean system. *J. Meteorol. Soc. Jpn.*, **78,** 441–460

Watanabe, M. and Nitta, T. 1998 Relative impacts of snow and sea surface temperature anomalies on an extreme phase in the winter atmospheric circulation. *J. Climate*, **11,** 2837–2857

Weng, W. and Neelin, D. 1998 On the role of ocean–atmosphere interaction in midlatitude interdecadal variability. *Geophys. Res. Lett.*, **25,** 167–170

Whitaker, J. S. and Sardeshmukh, P. D. 1998 A linear theory of extratropical synoptic eddy statistics. *J. Atmos. Sci.*, **55,** 237–258